Optimization of event selection and fake background estimation in a search for heavy scalars in dilepton final states with the ATLAS detector

Marius Burman Ingeberg

Supervised by Else Lytken and Yesenia Hernández Jiménez

Duration of Project: 11 Months

Thesis submitted for the degree of Master of Science

LUND UNIVERSITY

Department of Physics

Division of Particle Physics

December 2020

Abstract

The discovery of the Higgs boson h in 2012 further confirmed the remarkable accuracy of the Standard Model (SM). Despite this, some compelling excesses in multi-lepton final states were recorded in both major runs of the Large Hadron Collider (LHC). The excesses can be explained by the introduction of a model where a heavy boson X decays into a SM Higgs boson h and a singlet scalar S with Higgs-like couplings. The h and S subsequently produce opposite-sign different flavor lepton final states. Due to the plethora of SM processes producing similar final states, an accurate selection of events produced in the LHC is essential. This thesis investigates the optimization of the event selection using the full LHC Run 2 data recorded using the ATLAS detector at a centre-of-mass energy of 13 TeV, with the corresponding luminosity of 139 fb^{-1}. An investigation of the lepton isolation is conducted, where the highest performing working point is selected. In order to further suppress background, an event selection is constructed using a multidimensional signal significance scan. Finally, the background due to misidentified leptons is estimated using a data-driven method.

Acknowledgments

First I would like to express my genuine gratitude to Prof. Else Lytken for giving me the opportunity to conduct my master's thesis at Lund University. I would also like to thank her for the unwavering support and supervision, despite the circumstances this year offered.

I would also like to thank Dr. Yesenia Hernández Jiménez for her excellent supervision and for always being accessible to answer any question I might have. Your patience and support is much appreciated.

Finally I would like to express my sincere gratitude to my friends and family for giving me endless support. You keep me ever motivated and inspired.

Nomenclature

Acronyms	Meaning
ALICE	A Large Ion Collider Experiment
ATLAS	A Toroidal LHC ApparatuS
BR	Branching ratio
BSM	Beyond standard model
CERN	European Org. for Nuclear Research
CMS	Compact Muon Solenoid
CP	Charge parity
CR	Control region
CSC	Cathode strip chamber
DAQ	Data acquisition
DCS	Detector control system
EM	Electromagnetic
ggf	Gluon fusion
HEC	Hadronic end-cap calorimeter
HLT	High level trigger
htt	Top-associated production
IFF	Isolation and Fake Forum Group
ID	Identified
JVT	Jet vertex tagger
LAr	Liquid argon
LHC	Large Hadron Collider
LHCb	Large Hadron Collider beauty
MC	Monte Carlo
PBS	Proton Synchrotron Booster
PDF	Parton distribution function
QCD	Quantum chromo dynamics
QED	Quantum electro dynamics
QFT	Quantum field theory
RoI	Region of interest
RPC	Resistive plate chambers
SPS	Super proton synchrotron
TGC	Thin Gap Chamber
TRT	Transition radiation tracker
VBF	Vector boson fusion
Vh	Higgs-strahlung
SCT	Semiconducting tracker
SM	Standard Model
SR	Signal region

Symbols	Meaning
X	Heavy scalar
S	Higgs-like scalar
h	Higgs boson
W	W-boson
Z	Z-boson
γ	Photon
g	Gluon
u	Up quark
d	Down quark
s	Strange quark
c	Charm quark
t	Top quark
b	Bottom quark
e	Electron
μ	Muon
τ	Tau lepton
ν_e	Electron neutrino
ν_μ	Muon neutrino
ν_τ	Tau neutrino
fb^{-1}	Inverse femtobarn
$\sqrt{s}$	Centre of mass energy
p_{T}^{ll}	Transverse momentum
m_{ll}	Dilepton invariant mass
m_{T}	Transverse mass
E_{T}^{miss}	Missing transverse energy
R_{ll}	Angular separation
ϕ_{ll}	Azimuthal angle
η	Pseudorapidity

Contents

1 Introduction

The idea that fundamental building blocks constitute the universe has been around for millennia, and is still generally accepted today. Though the building blocks have for long time been a mystery, much light has been shed on the matter since the discovery of the atom. In the last 50 years there has been tremendous progress due to the introduction of the Standard Model (SM), which attempts to describe all fundamental matter and interactions. It is to this day one of the most powerful models, with impressive predictive power despite having a few glaring weaknesses. For example, the SM describes three of the four fundamental forces with great accuracy, but gravity is excluded from the theory. Due to having great predictive power while at the same time being incompatible with other observations, there is great incentive to extend the SM. This thesis focuses on one such extension.

With the discovery of the Higgs boson h by both the ATLAS and CMS experiments [1, 2] in 2012, many opportunities to study new physics have opened up. A large number of collaborations at the Large Hadron Collider (LHC) conduct massive experiments in order to investigate extensions of the SM. One such extension predicts the existence of a heavy boson X that decays into h and a singlet scalar S. The h and S bosons can then decay into a pair of different flavor opposite-sign leptons. As many SM processes produce similar final states, the signatures of X and S decays are exceedingly difficult to detect. This thesis focuses on the optimization of the selection of events in order to suppress background contribution and maximize signal yields, as well as the estimation of background due to misidentified leptons in the W+jets process. The analysis uses the LHC Run 2 data recorded by the ATLAS detector [25] at a centre-of-mass energy of 13 TeV with a luminosity of 139 fb^{-1}.

1.1 Outline of Thesis

Three separate studies were performed for the optimization. In order to reduce the amount of misidentified leptons that enter the analysis, constraints on the isolation of a lepton can be requested. There exists a variety of isolation working points, where the optimal choice is dependent on the analysis. The optimization of isolation working points in this analysis is described in Section 6.1. The selection of events based on kinematic quantities is also a useful tool to suppress the background. The optimization of the event selection is done using a multidimensional scan, and is described in Section 6.2. The misidentification of

leptons due to detector dynamics is difficult to model using Monte Carlo (MC) simulations. The rate of misidentification therefore needs to be accounted for in other ways, and is predicted using the Fake Factor method. This method is explained in Section 7. A brief introduction the SM is given in Section 2 along with an introduction of the X and S bosons. Section 3 provides background of the LHC and the ATLAS experiment, with some introduction to the coordinate system and the kinematic variables. The data and MC samples are specified in Section 4 and the reconstruction of objects along with the pre-selection are described in Section 5. Finally, Section 8 offers a summary and conclusion of the thesis.

2 Theoretical Background

2.1 The Standard Model

The SM [3, 4] is the current best attempt at describing the fundamental structures of the universe. Many of the theoretical building blocks were formulated by numerous scientists from all over the world during the 20th century, and it was not until 1978 that the current view of the SM was formulated [3]. Since then, the discovery of the top quark [5], the tau neutrino [6] and the Higgs boson have further established the SM as the current theory of everything. Despite the overwhelming success of the theory, it also has a few glaring weaknesses. The main limitations of the SM include the inability to describe gravity as the forth fundamental force, the matter/antimatter asymmetry problem, the exclusion of dark matter, and the seemingly ambiguous masses of some of the fundamental particles [7]. Because of this dichotomy of being one of the most accurate theories while simultaneously having obvious flaws, there is great incentive to further investigate the theory and its extensions. Phenomena that can not be explained using the SM as well as theories that go beyond the SM are usually called *Beyond Standard Model* (BSM) physics. This thesis will investigate such BSM physics after a brief overview of the SM in its current state.

2.1.1 The Elementary Particles of the Standard Model

Elementary particles are particles that thus far has shown no further internal structure. They are according to current understanding the fundamental building blocks of all matter. A collection of all particles of the SM can be seen in Figure 1. Each particle has a unique set of intrinsic properties such as electric charge, mass and spin. The spin of a particle represents an intrinsic angular momentum and is usually used to divide the particles of the SM into two main categories; the *fermions* and the *bosons*.

2.1.2 Fermions

The fermions are half-integer spin particles ($\frac{1}{2}$, $\frac{3}{2}$, $\frac{5}{2}$...) which means they follow the *Pauli Exclusion Principle*. The Pauli Exclusion Principle forbids any two fermions from being in the same quantum state. This allows the fermions to be the building blocks of the ordinary matter we see around us as no fermions can collapse into the same point in space time. The fermions are additionally divided into two groups known as the *quarks*

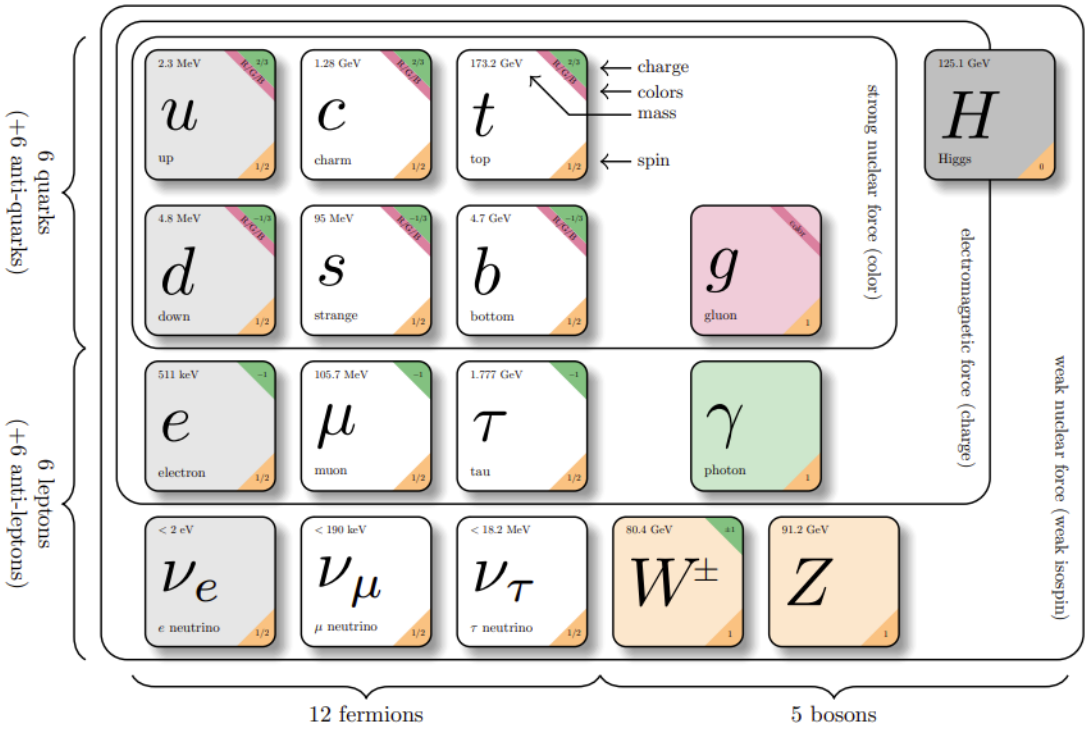

Figure 1: The elementary particles and the force carriers of the SM. Modified from Ref. [8].

and the *leptons*. There are six quarks that come in three different families. The first family consists of the up (u) quark with an electric charge $q = 2/3$ and the down (d) quark with $q = -1/3$. Different combinations of these quarks make up the protons and neutrons which form the core of atoms, meaning only these two quarks make up a majority of the world we inhabit. The other families retain similar structure as the first family, but with increasing mass for each quark. The next family thus consists of the charm (c) and strange (s) quark and the final family consists of the top (t) and bottom (b) quark. The top is the heaviest quark with a sizable mass of $m_{top} = 173.2$ GeV compared to the up quark, being the lightest quark at $m_u = 2.3$ MeV.

Quarks cannot be observed alone due to a phenomenon known as color confinement, meaning they always form composite particles known as *hadrons*. Different combinations of quarks allow a vast variety of hadrons to exist, most of which are unstable. In fact, only the proton and neutron are observed to be stable for any meaningful amount of time inside atomic nuclei, which is why they make up most of the matter around us.

As in the case of the quarks, the leptons also exhibit this pairwise structure where they can be divided into families. In each family there is a charged lepton and its associated neutral neutrino. The charged leptons are the electron (e^-), the muon (μ^-) and the tau-lepton (τ^-) and they have the associated neutrinos electron neutrino (ν_e), muon neutrino

(ν_μ) and tau neutrino (ν_τ) in their respective family. The charged leptons have similar properties to each other except for their significant differences in mass. The heavier charged leptons thus decay very quickly leaving the electron as the only stable charged lepton. The remaining leptons are the elusive neutrinos, the reason for which will be discussed in short. Although observed to have some low but non-zero mass, the SM in its current states predicts them to be massless [4].

This concludes the fermions of the SM with one important exception; each particles has an antiparticle associated with it. An antiparticle has identical mass of the original particle, but with opposite charge. A particle-antiparticle pair in contact can annihilate each other producing new particles, often a pair of photons.

2.1.3 Bosons

In general it is said that there are four fundamental forces which the fermions interact via; *the strong force*, *the weak force*, *the electromagnetic force* and *gravity*. As in the case of the mass of the neutrinos however, gravity is not included in the SM despite its apparent existence and will not be dealt with here. The remaining three forces are mediated by the gauge bosons shown in color in Figure 1. All gauge bosons possess a spin of 1, giving them the name *vector bosons*. The mediation of force through the gauge bosons is responsible for all interaction and subsequently the binding of particles. In the following section each force will be described briefly.

The electromagnetic force is mediated by the photon (γ) and is responsible for everything from magnets to flashlights. It is the force that is at the core of all modern electronics, as well as being responsible for binding atoms together. Since the photon is a massless particle, the range of the electromagnetic force tends to the infinite. It affects all particles except the neutrinos. The electromagnetic force is usually described by the theory of quantum electrodynamics (QED).

The weak force is unique as it has three bosons associated with it; the charge neutral Z boson (Z) and the charged W bosons ($W^\pm$). The weak force is responsible for phenomena such as radioactive decay of atoms and fission. Due to the relatively high mass of the Z and $W^\pm$ bosons, the range of the weak force is rather short. It can be approximated to only reach about 0.1% of the diameter of a proton [9]. Despite being a rather short and weak force, it does affect all particles of the SM. As can be seen in Figure 1, the neutrinos are the only fermions which are only affected by the weak force. This means that their probability of interaction is very low, making them substantially difficult to measure in

experiments.

The strong force is mediated by the gluon (g) and it only affects the quarks and the gluons themselves. Because of its considerable strength and short range compared to the other forces, it is often said that the gluons *glue* quarks together to form the previously mentioned hadrons. Multiple hadrons can also come together under the strong force to form atomic nuclei.

2.2 The Higgs Boson

The most recent addition to the SM is the h boson. [4] [10]. It is a result of a mechanism for spontaneous breaking of gauge symmetries that was first proposed in 1964 by Englert & Brout, Higgs and Guralnik et al. [10, 11]. The theory helped explain why the gauge bosons of the weak force had such high mass compared to the massless bosons of the electromagnetic and strong force. An ever-permeating complex scalar quantum field that spans the entire universe was postulated and the excitation of this field into a quantum would be known as the Higgs boson. Such postulation of an ever-permeating field might seem arbitrary but in fact such field is one of the fundamental assumptions of *Quantum Field Theory* [12] (QFT), one of the theories the SM is based upon. Despite the wide success of QFT, it predicted the masses of the gauge bosons to be zero which was considered unreasonable. The addition of the Higgs field which the gauge bosons couple to gave a solid explanation as to where they obtain their mass from. Intuitively the field is often explained analogous to a viscous fluid which the particles have to traverse, and the more the particles interact with the fluid the more massive they appear. In other words; the mass of the particles is proportional to the coupling strength to the Higgs field, explaining the difference in mass between the gauge bosons. Likewise, the masses of the fermions are also generated from the Higgs field through something called *Yukawa interaction*.

There exists a multitude of possible production mechanisms for the Higgs boson although the probability of producing it in any given collision is low. The four most common production mechanisms can be seen in Figure 2 where the most dominant one is *gluon fusion* (ggf). Here two gluons interact via the exchange of a virtual top quark to produce a Higgs boson. The second most common production mechanism is the *vector boson fusion* (VBF) where two (anti-)quarks are scattered through the exchange of a Z or W boson, of which a Higgs boson can be radiated off. The third most relevant production mechanism is known as *Wh- and Zh-associated production* or *Higgs-strahlung* (Vh). This is a result

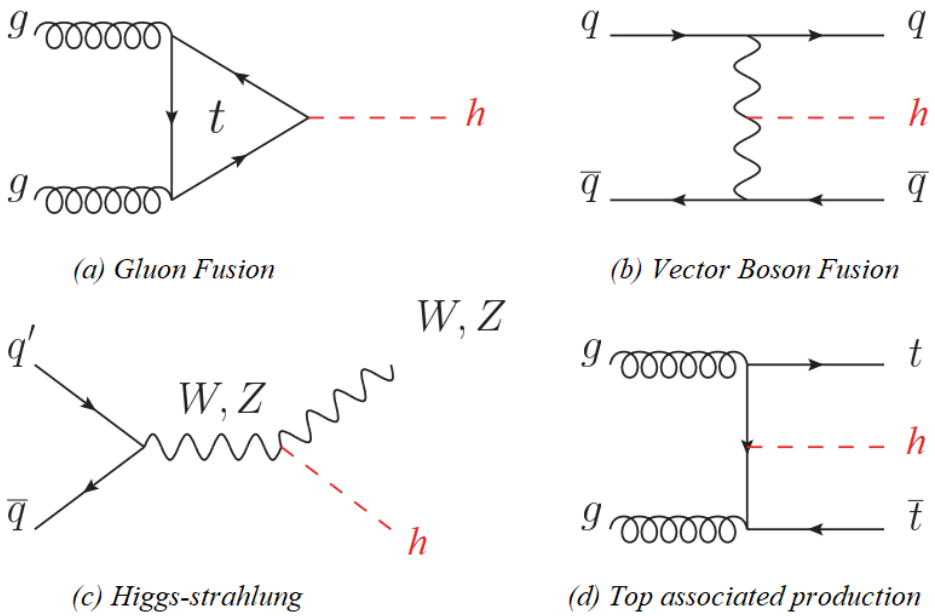

Figure 2: Feynman diagrams for the four most prevalent production mechanisms of the Higgs boson. Modified from Ref. [4].

of a collision between a quark and an anti-quark, producing a Z or W boson which can emit a Higgs boson. Finally, there is the *top associated production* (htt) where the Higgs boson is radiated from the production of top quarks.

2.3 Beyond Standard Model Physics

2.3.1 Heavier Scalar Bosons

The first Higgs bosons were discovered in 2012 at the LHC by both the ATLAS [1] and CMS [2] experiments. The measurements were found to be consistent with the predictions which further established the accuracy and predictive power of the SM. Despite this, some statistically significant excesses were found in the data obtained during the Run 1 period of the LHC [13]. As discussed in references [13–17], the introduction of a heavy scalar X could explain many of the anomalous features. The results in Ref. [13] show that with only the parameter β_g^2, which is the scale factor for the production cross section of X, their data could be fit with a significance of 3σ. They also found that the best fit mass of X was $m_X = 272^{+12}_{-9}$ GeV.

Another scalar boson S was further postulated as a potential decay product of X,

allowing X to decay into SS, Sh and hh. The mass of S is usually studied in the mass range $m_h < m_S < m_X - m_h$ where $m_h = 125$ GeV is the mass of the Higgs boson, m_S is the mass of S and m_X is the mass of X, usually fixed to $m_X = 270$ GeV. For the Run 1 data, the best fit mass of S was found to be $m_S = 150$ GeV. The S boson is assumed to not be directly produced in collisions, but instead through the decay of X. The dominant decay channel for the production of S is assumed to be $X \to Sh$, which is the focus of this thesis, is usually simplified to have a 100% branching ratio (BR). The prevalent production channels for X and its subsequent decay modes into Sh can be seen in Figure 3.

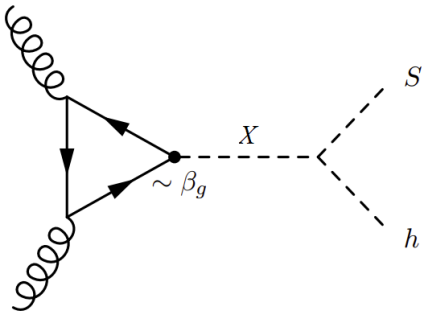

(a) Gluon fusion (ggF).

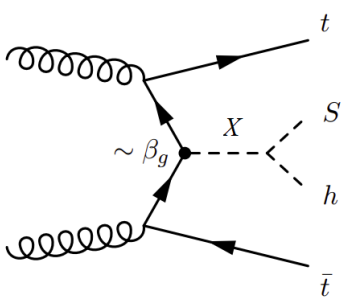

(b) Top pair associated production (ttH).

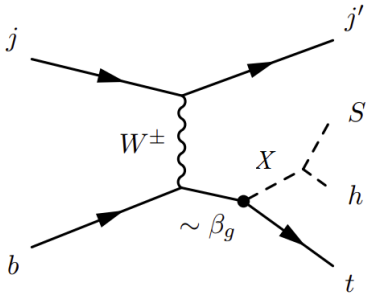

(c) Single top associated production (tH).

Figure 3: Feynman diagrams for the most prevalent production modes of X and its decay modes into Sh. Modified from Ref. [16].

2.3.2 Multi-lepton Final States

The end of Run 2 in December 2018 at the LHC [31] introduced a larger set of data with improved statistics allowing for further investigation of the previously described excesses. In general, most features of the data that sparked the investigation of heavier scalar bosons persisted or were magnified [15]. This created greater incentive to further investigate the possibility of heavier scalar bosons. As in the case of the Higgs boson, neither X nor S can

be observed directly in a detector and one has to instead examine their decay products. As stated earlier, S is a decay product of X meaning that one has to ultimately examine the decay products of S. There exist some models of this decay out of which this thesis will focus on a *Higgs-like S model* where S is assumed to have globally re-scaled Higgs-like couplings [15]. Here the couplings are assumed to be suppressed by some yet undefined BSM physics resulting in a Higgs-like coupling hierarchy to the Standard Model particles. This results in a relatively small cross section of the S, although its BRs are the same as a higher-mass Higgs boson. In this model, S decays prevalently to W and Z boson pairs as m_S approaches $\sim 2m_W$. The BRs as a function of the mass of h can be seen in Figure 4. The S boson will thus produce multi-lepton final states, mostly through the decay of W and Z bosons. In this analysis, only electron and muon final states will be considered due to the increasing complexity resulting from the combinatorics of three lepton flavors.

Three different mass points for the X and the S are considered. Preferably the entire range of plausible masses for the bosons would be scanned, but because of limitations on the amount of signal samples that can be requested, the analysis has to be restricted to three choices. The selected signal mass point configurations can be seen in Table 1.

Table 1: Mass configuration of the three signal mass points used in this analysis.

Notation	m_X [GeV]	m_S [GeV]
$X240S170$	240	170
$X350S240$	350	240
$X400S240$	400	240

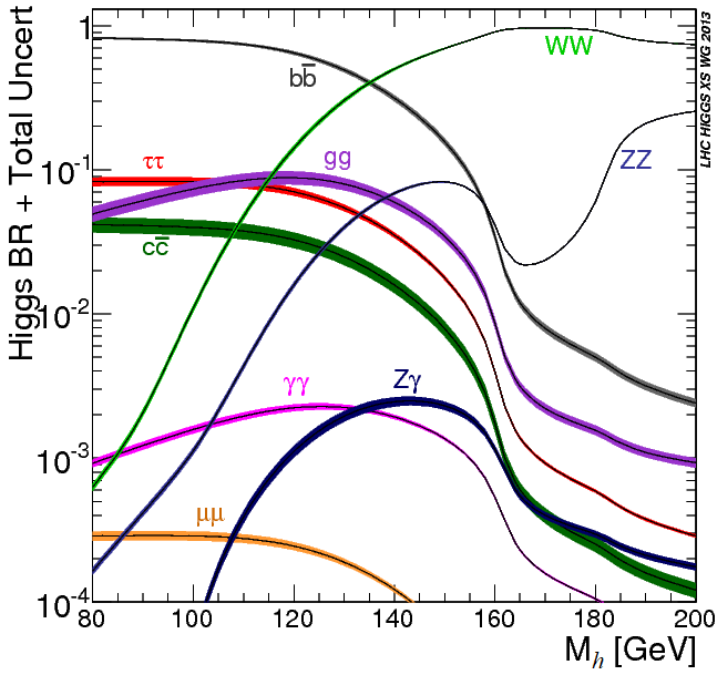

Figure 4: Branching ratios and total width of the SM Higgs boson. Ref. [18].

3 Experimental Background

3.1 The Large Hadron Collider

The Large Hadron Collider [20] is the world's largest particle collider and is hosted by the European Organization for Nuclear Research (CERN). It is a two-ring circular accelerator that forms a ring with a circumference of 27 km deep underground under the French-Swiss border outside Geneva. Two beams of protons or heavy ions are accelerated in a counter-rotating fashion at velocities approaching the speed of light. The beams are then focused such that they collide with each other at four designated interaction points where the collisions can be recorded. Extreme energies are required to produce massive particles, and higher energies allows for increasingly massive particles to produce. The LHC is therefore continually upgraded to increase the energy, often measured as centre-of-mass energy, denoted $\sqrt{s}$. Run 1 of LHC started out at $\sqrt{s} = 7$ TeV in 2010-2011 but was upgraded in 2012 to achieve $\sqrt{s} = 8$ TeV [30]. The second run of LHC was operated at $\sqrt{s} = 13$ TeV in the period 2015-2018 [31].

In order to accelerate protons to such high $\sqrt{s}$, they need to already have sufficient energy when they enter the main rings. The process of producing protons with high enough energy is a complicated multi-step process that briefly will be described here. The protons are produced by stripping the electrons off hydrogen gas allowing them be accelerated in a linear accelerator called Linac2. In this first step they are accelerated to an energy of 50 MeV. Subsequently, the protons are directed to the Proton Synchrotron Booster (PBS) where they are further accelerated to an energy of 1.4 GeV. The next step is the Super Proton Synchrotron (SPS) where the protons reach an energy of 450 GeV. At this point the protons have high enough energy to be injected into the LHC where they are finally accelerated up to 6.5 TeV in each direction to be able to produce the final centre-of-mass energy at $\sqrt{s} = 13$ TeV. A schematic view of the aforementioned accelerators can be seen in Figure 5 along with the LHC and other accelerators and experiments.

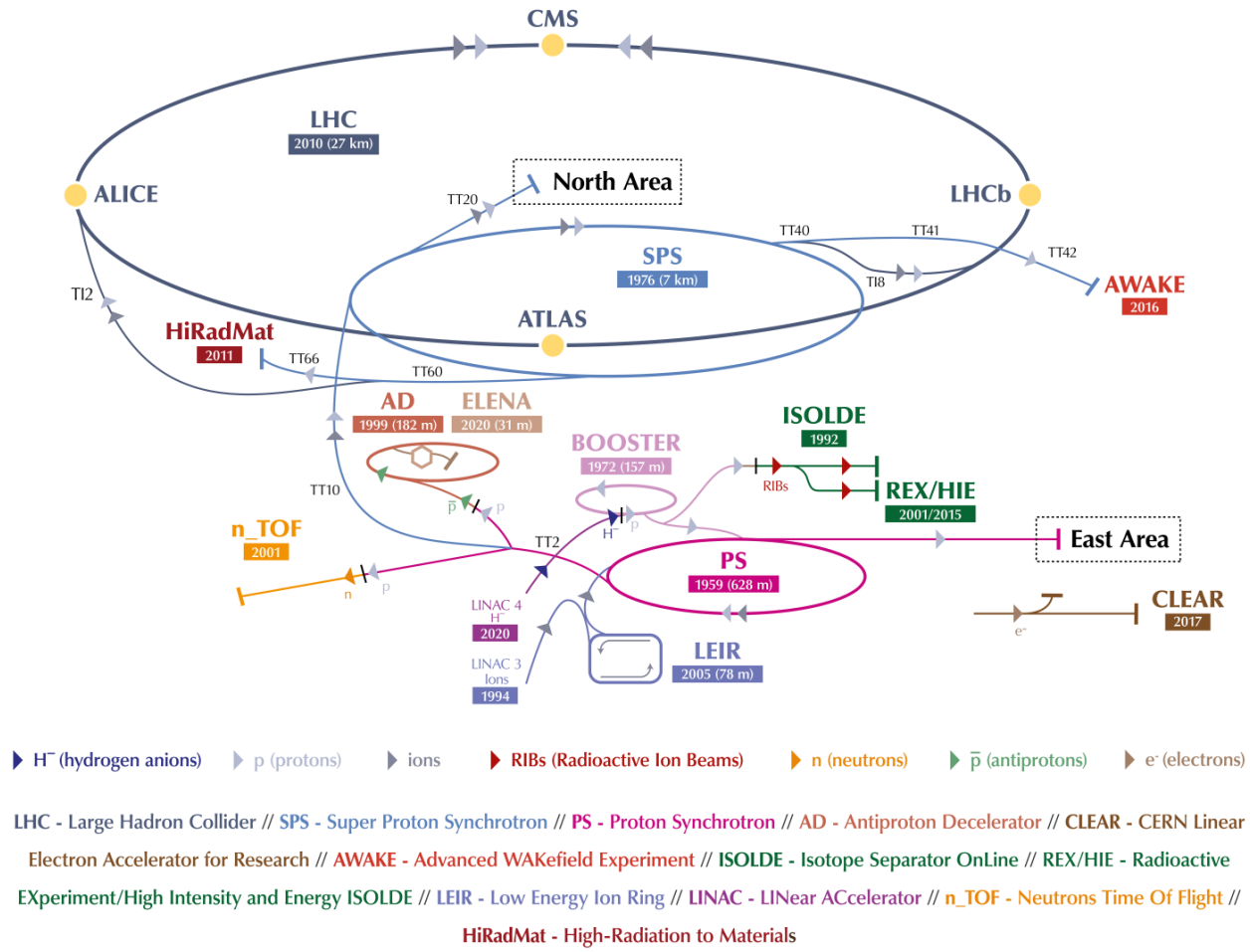

Figure 5: Schematic view of the Large Hadron Collider and its neighboring experiments and accelerators. Ref. [21].

In order to detect and record the collisions from the protons or heavy ion beams, four major experiments are stationed along the LHC as seen in Figure 5. A brief explanation of each experiment will be given here. The ALICE (A Large Ion Collider Experiment) experiment [22] is a general purpose and heavy-ion detector. It focuses on strongly interacting matter and quark-gluon plasma at extreme energy densities and temperatures in nucleus-nucleus collisions. It is therefore mostly used to examine Pb-Pb and Pb-p collisions. The LHCb (Large Hadron Collider beauty) experiment [23] is devoted to precise measurements of CP violation and rare decays of beauty and charm hadrons. For this reason, the detector geometry differs from the other experiments as its a single-arm forward spectrometer. This is because at high energies b hadrons are produced in the same forward or backward cone, close to the beam line. The CMS (Compact Muon Solenoid) experiment [24] hosts a multi-purpose detector which is used for various searches and investigations. It is often used in tandem with the ATLAS (A Toroidal LHC ApparatuS)

experiment [25], also a general purpose detector, as they can offer extensions and support each other. The next section offers a more detailed description of the ATLAS experiment as it provided the data used in the analysis of this thesis.

3.2 The ATLAS Experiment

The ATLAS detector [25] is the largest general purpose detector at the LHC. Because of this, it is designed to be utilized for a variety of investigations such as the search for supersymmetry, new heavy W- and Z-like bosons, exotic Higgs bosons as well as high precision measurements of electroweak interactions, QCD and flavor physics. The detector is therefore optimized to be able to measure a broad range of physics processes, which results in it having a layer-like structure made of many high precision instruments. It is constructed in a cylindrical shape centered around the beam line and is 25 m in height and 42 m long weighing roughly 7000 tonnes. It is forward-backward symmetric relative to the interaction point. In order to reconstruct and identify charged particles it uses a tracking system, allowing for the measurement of particle momentum, identification of electrons and photons, and jet tagging. The calorimeters of ATLAS allow for accurate energy measurements of hadronic and electromagnetically interacting particles. The calorimeters are surrounded by muon spectrometers, used for the measurement of muons. The detector layout can be seen in Figure 6. The following sections describe the subsystems of ATLAS in further detail.

3.2.1 The Coordinate System and Kinematic Variables

In order to properly measure and track particles, a coordinate system is constructed where the interaction point is defined as the origin and the z-axis is defined along the beam line [25]. The x-y plane is transverse to the beam direction where the x-axis is pointing from the interaction point to the centre of the LHC while the y-axis is pointing upwards. Cylindrical coordinates are also used in the transverse plane where ϕ is the azimuthal angle, measured around the beam axis, and the polar angle θ is the angle measured from the beam axis. The pseudorapidity η is often used as a measurement of angle from the beam line, and is defined as

$$\eta = -\ln \tan(\theta/2). \tag{1}$$

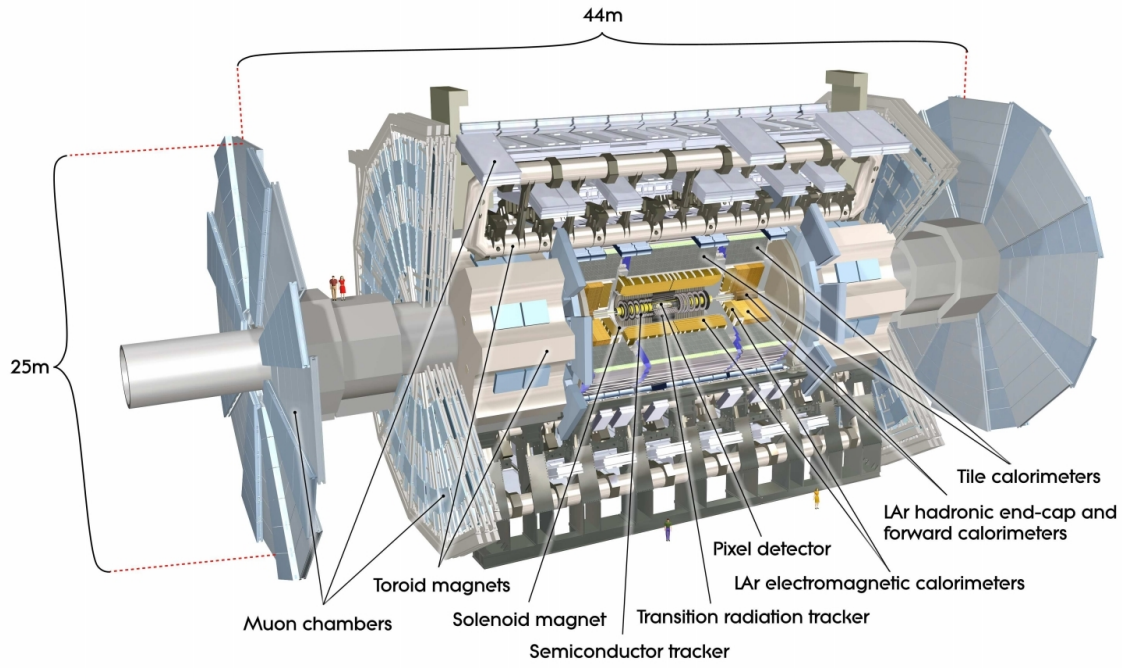

Figure 6: Cross-section view of the ATLAS detector. Ref. [25].

It is zero for particles moving directly perpendicular to the beam line ($\theta = 90^o$) and approaches infinity for particles moving along a small polar angle. The angular separation between particles is defined as

$$\Delta R = \sqrt{\Delta\eta^2 + \Delta\phi^2} \tag{2}$$

where $\Delta\eta$ and $\Delta\phi$ are the differences in azimuthal angle and pseudorapidity between the particles.

It is often advantageous to define some kinematic variables using the transverse components in the x-y plane due do being invariant under Lorentz boosts in the z direction. The missing transverse energy $E_{\mathrm{T}}^{\mathrm{miss}}$ is a measurement of the missing energy of the system due to particles not interacting with elements of the detector. This can be a result of weakly or non-interacting particles such as neutrinos, or malfunctions in the detector. It is defined as

$$E_{\mathrm{T}}^{\mathrm{miss}} = \sqrt{(E_{\mathrm{T}}^{\mathrm{x}})^2 + (E_{\mathrm{T}}^{\mathrm{y}})^2}. \tag{3}$$

Similarly, the transverse momentum

$$p_{\mathrm{T}} = \sqrt{(p_{\mathrm{x}})^2 + (p_{\mathrm{y}})^2}, \tag{4}$$

is defined as the momentum perpendicular to the beam axis. Together these two kinematic variables can be used to express the transverse mass, which is defined as

$$m_{\mathrm{T}} = \sqrt{2p_{\mathrm{T}}E_{\mathrm{T}}^{\mathrm{miss}}(1-\cos\phi)}. \tag{5}$$

3.2.2 The Inner Detector

The first detection system surrounding the beam line is called the inner detector [25]. It tracks charged particles above $p_T > 0.5$ GeV and within the pseudorapidity range $|\eta| < 2.5$ and provides accurate momentum resolution, primary and secondary vertex measurements, charge identification and the direction and origin of tracks. It is also used to identify electrons with pseudorapidities of $|\eta| < 2.0$ and energies between $0.5 - 150$ GeV. The inner detector comprises of three independent sub-detectors at different radii with respect to the beam line. The Transition Radiation Tracker (TRT) is the outmost sub-detector system, enveloping the Semiconducting Tracker (SCT) system which in turn envelops the silicon pixel detector (Pixel). All subsystems take on a cylindrical shape in a layered structure around the beam line, and are in turn enveloped by a 2 T solenoid magnetic field. The general layout of the inner detector can be seen in Figure 7.

Because of the massive flux of particles (high luminosity) close to the interaction points, the Pixel detector is designed to have very high granularity. It is therefore well suited for impact parameter- and vertex reconstruction, which is essential for identifying the origin of the initial collision as well as measuring secondary vertices's resulting from the decay of primary particles. It is also used for b-tagging, which is a method for identifying jets originating from b quarks and distinguishing them from jets originating from lighter quarks. The Pixel detector contains a total of 1744 identical pixel sensors. The external dimensions of each pixel sensor is 19×63 mm^2, though the nominal pixel size ends up at 50×400 μm^2 due to readout electronics. Each sensor contains 47323 pixels but because of limited space there are a total of 406080 readout channels. In total, the Pixel detector contains over 80 million readout channels.

The SCT [26] surrounds the Pixel detector and is important for accurate measurements of momentum, but also help in the measurements of impact parameter and vertices. It consists of a total of 4088 modules of silicon-strip detectors out of which 2112 modules are contained in the barrel region where they are stacked in four cylindrical layers. The remaining modules are contained in two end-caps each containing nine stacked disc-like layers.

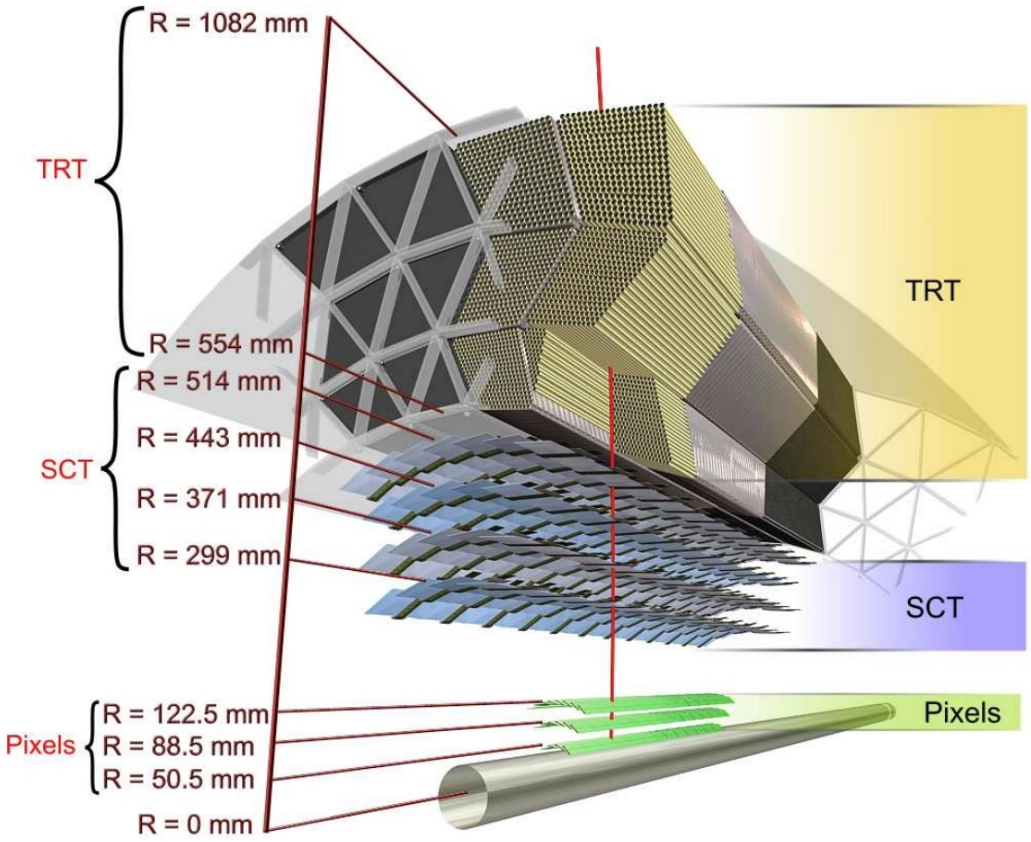

Figure 7: Drawing of the detector elements and structural components of the inner detector. Ref. [25].

The final subsystem of the inner detector is the TRT [27], which consists of 300000 straw detectors packed closely together parallel to the beam line. Each straw detector is a drift tube with a diameter of 4 mm containing a xenon-based gas mixture that allows for production of transition radiation from passing charged particles. The transition radiation is a result of charged particles crossing boundaries of media with different dielectric constants. The TRT exploits the fact that the probability of emitting transition radiation for a given particle is proportional to its Lorentz γ-factor, and is used to distinguish electrons and pions having a p_{T} up to 100 GeV, along with identification of other particles.

3.2.3 The Calorimeter Systems

The ATLAS calorimeters [25] surround the inner detector and are used to measure the energy of particles and jets as well as the missing transverse energy. They consist of sampling detectors with ϕ-symmetry, providing full coverage around the beam line. The detectors have layered structure with alternating active and passive absorbing materials. Incoming particles create electromagnetic or hadronic showers of secondary particles in

the absorbing material which can be detected using the active layers allowing for accurate measurement of energy. The absorbing materials interact independently of the charge of particles, meaning that energies of neutral particles such as neutrons can also be measured. There are two kinds of calorimeters in ATLAS, one is optimized for electromagnetic interactions and the other hadronic interactions. The different calorimeter systems can be seen in Figure 8.

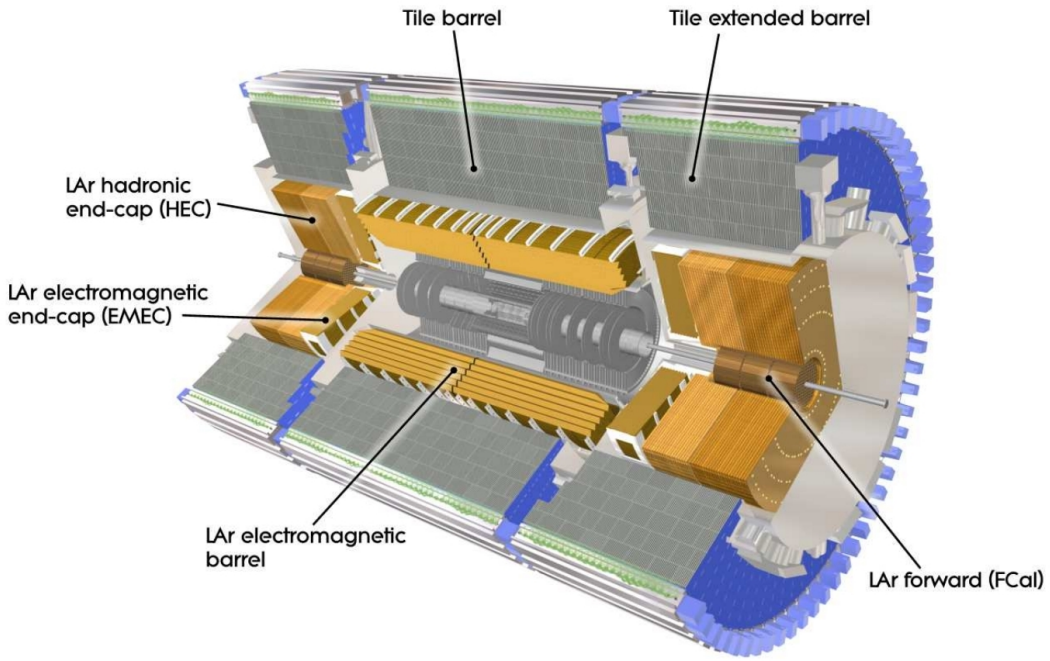

Figure 8: Cut-away drawing of the ATLAS calorimeters. Ref. [28].

The electromagnetic calorimeter consists of high-granularity elements and is divided into a barrel ($|\eta| < 1.475$) and two end-caps ($1.375 < |\eta| < 3.2$). It uses liquid argon as the active layer and lead as the passive layer. The lead absorbs the energy of particles that interact electromagnetically, mainly photons and electrons causing them to deposit energy in different forms depending on the particle. For example, electrons emit bremsstrahlung and photons convert to e^+e^- pairs forming electromagnetic showers. The charged particles can then enter a layer of liquid argon, creating a trail of ionization which can be read as an electrical signal. Hadrons and muons pass in a relatively non-interacting manner while neutrinos pass directly through as they only interact weakly.

The hadronic calorimeter is placed directly outside of the electromagnetic calorimeter. It measures the energy and direction of particles that pass through the electromagnetic calorimeters, such as hadronically decaying leptons and jets. The hadronic calorimeter consists of three calorimeter systems: the tile calorimeter (TileCal), the liquid argon (LAr)

hadronic end-cap calorimeter (HEC) and the LAr forward calorimeter (FCal). The TileCal barrel covers the region $|\eta| < 1.0$ along with its extended barrels that cover the region $0.8 < |\eta| < 1.7$. It uses steel as its absorbing layers and plastic scintillating tiles as the active layers. When a charged particle passes through the scintillators, valence electrons are excited which emit excess energy as photons. These photons are then detected and amplified using photomultiplier tubes which create a signal. The HEC consists of two wheels per end-cap and covers the region $1.5 < |\eta| < 3.2$ where liquid argon is used as the active medium and copper as the passive absorber. The FCal is situated in the forward region and covers the range $|\eta| < 4.9$. It consists of three modules where the first uses LAr and copper as the active and passive layers while the remaining modules use tungsten as the passive layer.

3.2.4 Muon Spectrometer

The outmost detector system at ATLAS is the muon spectrometer [25]. The only particle that in principle travels through the preceding detector systems (with the exception of non- or weakly interacting particles like neutrinos) is the muon, and thus a separate muon spectrometer is required. It consists of four subsystems that together perform high precision tracking and triggering. The tracking is made possible by the muon system being contained in a toroidal magnetic field of $\sim$ 0.5 T inside the barrel and $\sim$ 1 T at the end-caps. Monitored Drift Tubes (MDT) and Cathode Strip Chambers (CSC) are used for high precision tracking in the barrels and end caps respectively, covering the range $|\eta| < 2.7$. Resistive Plate Chambers (RPC) are used as triggers inside the barrel ($|\eta| < 1.05$) while Thin Gap Chambers (TGC) are used as triggers at the end caps ($1.05 < |\eta| < 2.4$). The different subsystems are highlighted in Figure 9.

3.2.5 Data Collection and Triggers

The collection of data is a complicated process that requires multiple systems because of the high luminosities at ATLAS. The Data Acquisition (DAQ) system, the Detector Control System (DCS) and the timing- and trigger-control logic systems are all used in the data acquisition and they are all in turn partitioned into subsystems [25].

The trigger system of ATLAS consists of two levels: a hardware-based first level (L1) and a software-based high level trigger (HLT). The L1 trigger runs with a latency of 2.5 μs which reduces the event race from the LHC interaction rate from approximately 40 MHz to 100 kHz [29]. For every measured event, the L1 trigger defines Regions-of-Interests

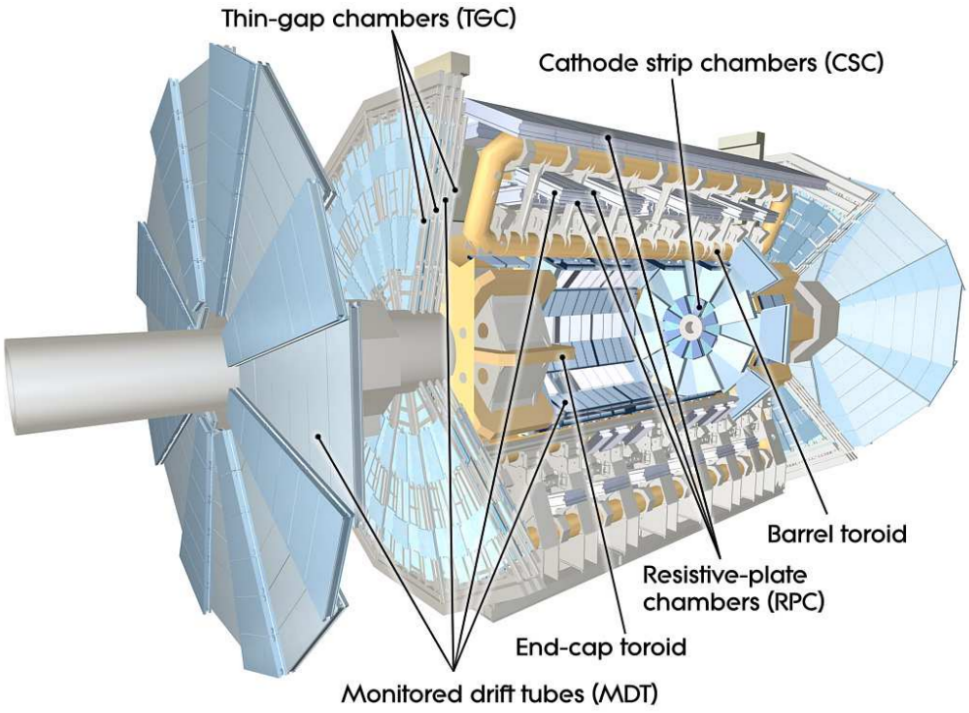

Figure 9: Conceptual layout of the ATLAS muon system. Ref. [25].

(RoI) using the coordinates η and ϕ to record regions where potentially interesting features were identified. The RoI data contains information about identified features and what criteria was passed, and is subsequently passed to the HLT. The HLT consists of reconstruction algorithms that are run using approximately 40000 processor cores, allowing decisions to be made typically within 300 ms. It provides around 2500 independent trigger chains which are executed within the RoIs defined by the L1 trigger allowing for full-event reconstruction. Events that are accepted by the HLT are written into data streams to be used for detector calibration, trigger analysis and physics analysis.

4 Data and Simulation

4.1 Data

There has thus far been two major data acquisition periods at the LHC referred to as Run 1 [30] and Run 2 [31]. They were separated by a shut-down period of roughly three years dedicated to maintenance and upgrades to the LHC and the experiments. Run 1 operated at a centre-of-mass energy of $\sqrt{s}$=7-8 TeV in the period 2009-2012, reaching a recorded luminosity of 21.3 fb^{-1}. Run 2 operated at $\sqrt{s}$ = 13 TeV during the period 2015-2018, and provided the data used in this analysis. The luminosity delivered by the LHC was increased throughout Run 2 reaching as high as 153 fb^{-1}, out of which 146 fb^{-1} was recorded by ATLAS and 139 fb^{-1} was considered data of good quality [32]. The progression of the luminosities over the Run 2 period can be seen in Figure 10.

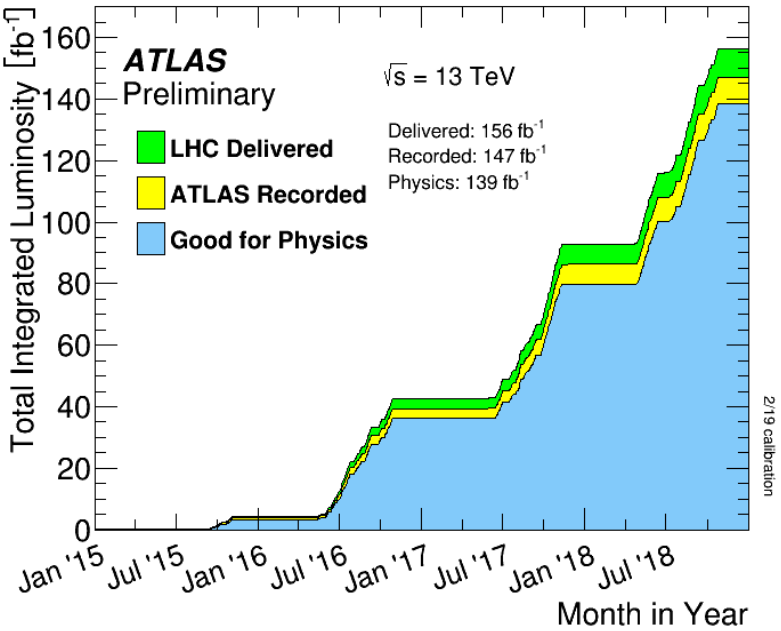

Figure 10: Progression of the total integrated luminosity in ATLAS during the Run 2 period. Ref. [33].

4.2 Background Samples

All processes that produce final state dileptons with opposite charge and different flavor contribute to the background. The most dominant contribution to the background comes from correctly identified SM processes although fake background and lepton charge misidentification must also be taken into account. Background and signal samples are

modeled using MC generators where the choice of generator is dependent on the process. The event generators and event generator settings used in this analysis are presented in the following section. A summary is presented in Table 2.

The production and decay of the Higgs boson are simulated for all main production modes: ggF, VBF, Vh and htt (see Section 2.2). The standard Higgs mass of $m_h = 125$ GeV is used for all samples. The samples are generated using POWHEG [34] + PYTHIA 8.210 [35] where the CTEQ6L1 [36] parton distribution function (PDF) is used with the AZNLO [37] tune.

Top quark associated events events are generated in two distinct ways. Samples including $t\bar{t}$ and tW are generated using POWHEG + PYTHIA8 while samples including $t\bar{t}W$, $t\bar{t}Z$ and tZ are generated using MADGRAPH5 [38] + PYTHIA8. In both cases, the NNPDF2.3LO [39] is used with the A14 tune [39]. The mass of the top quark is set to $m_t = 175.5$ GeV.

$W\gamma$ and $Z\gamma$ ($V\gamma$) samples are generated using SHERPA 2.2.8 [40] with the NNPDF3.0NNLO PDF and the SHERPA DEFAULT tune. The transverse momenta of both processes are required to be $p_{\mathrm{T}} > 7$ GeV, and the distance in the $\eta - \phi$ plane is restricted to $\Delta R > 0.1$. The leptons from the Z boson in the final states are also required to have $m_{ll} > 2$ GeV.

Triboson (WWW, WWZ, WZZ, ZZZ) and Diboson (WW, WZ, ZZ) samples are produced using SHERPA 2.2.2. In both cases, NNPDF3.0NNLO is used for the PDF with the SHERPA DEFAULT tune.

$W \to e\nu/\mu\nu/\tau\nu$+jets or simply W+jets samples are generated with POWHEG + PYTHIA8, using the CTEQ6L1 PDF with the AZNLO tune. In addition to MC samples, a data driven method is also used to model the W+jets processes more accurately and is described in Section 7. Z+jets events are produced with SHERPA 2.2.1 using the NNPDF3.0NNLO PDF and the SHERPA DEFAULT tune.

Table 2: Summary of the event generators, PDF's and tunes for the different background processes used in the $X \to Sh$ analysis.

Process	Event Generator	PDF	Tune
Higgs	POWHEG + PYTHIA8	CTEQ6L1	AZNLO
Top			
$t\bar{t}, tW$	POWHEG + PYTHIA8	NNPDF2.3LO	A14
$t\bar{t}W, t\bar{t}Z$, tZ	MADGRAPH5 + PYTHIA8	NNPDF2.3LO	A14
$V\gamma$	SHERPA 2.2.8	NNPDF3.0NNLO	SHERPA DEFAULT
Triboson	SHERPA 2.2.2	NNPDF3.0NNLO	SHERPA DEFAULT
Diboson	SHERPA 2.2.2	NNPDF3.0NNLO	SHERPA DEFAULT
W+jets	POWHEG + PYTHIA8	CTEQ6L1	AZNLO
Z+jets	SHERPA 2.2.1	NNPDF3.0NNLO	SHERPA DEFAULT

4.3 Signal Samples

The $X \to Sh$ signal samples are generated using PYTHIA 8.210 at leading order. NNPDF23LO is used for the PDF with the A14 tune. The samples are produced for the three different signal mass points described in Section 2.3.2 with the Higgs mass set to $m_h = 125$ GeV. The samples are produced such that they are inclusive of all possible decays of S and h. A multi-lepton filter is applied, requiring at least 2 leptons with transverse momentum $p_T > 8$ GeV in the region $|\eta| < 3$. The filter has an efficiency of $\sim$ 4-12%. Table 3 summarizes the settings for each signal mass point.

Table 3: Signal samples of the three different signal mass points for the $X \to Sh$ analysis.

Process	m_X, m_H [GeV]	Event Generator	PDF	Tune
$X \to Sh$	240, 170	PYTHIA8	NNPDF23LO	A14
	350, 240	PYTHIA8	NNPDF23LO	A14
	400, 240	PYTHIA8	NNPDF23LO	A14

5 Object Reconstruction and Pre-selection

In order to conduct an analysis, the electrical signals recorded by the detector systems described in Section 3.2 need to be reconstructed and identified. The $X \to Sh$ search focuses mostly on final state electrons, muons, jets and b-tagged jets. Their method of reconstruction and identification will be described in this chapter.

5.1 Leptons

The lepton selection in this analysis is conducted such that the rejection of fake lepton background is maximized while the loss in signal efficiency is minimized. Only leptons that originate from a primary vertex (see Section 3.2.2) are considered, and if there is more than one primary vertex for an event, only the one with the highest sum square of track Σp_{T}^2 is considered. In the primary vertex construction, only tracks which pass quality cuts with $p_{\mathrm{T}} > 500$ MeV are selected.

Misidentified leptons can cause significant contamination and need to be dealt with efficiently. This can be done by the exploitation of the impact parameter, which is determined by the point of closest approach between the primary vertex and a track [41]. There are two distinct kinds of impact parameter depending on its orientation in the 3D plane. The transverse impact parameter d_0 measures the distance between the point and the primary vertex in the x-y plane and the longitudinal impact parameter z_0 is the distance in the z plane along the beam axis. The significance of the transverse impact parameter is used for the selection, and is defined as $|d_0|/\sigma(d_0)$ where $\sigma(d_0)$ is the uncertainty in d_0. It is used to select for electrons with $|d_0|/\sigma(d_0) < 5$ and muons with $|d_0|/\sigma(d_0) < 3$. The longitudinal impact parameter is multiplied by $\sin\theta$ and its absolute value is required to be $|z_0 \sin\theta| < 0.5$ mm for both leptons.

In order to reduce the number of misidentified leptons, one can require criteria on the isolation. There exists a wide variety of isolation working points which are being regularly updated. The choice of isolation is dependent on the the details of the analysis, and the choice for this analysis will be detailed in Section 6.1.

5.2 Electrons

To be able to distinguish electrons from other objects such as photons and jets, identification and isolation requirements are used. The identification is based on a likelihood

method described in Ref. [42]. There are three levels of identification called *LooseLH*, *MediumLH* and *TightLH* with average identification efficiencies of 93%, 88% and 80% respectively. In this analysis, TightLH is used for electron with $p_{\mathrm{T}} < 25$ GeV and MediumLH is used otherwise. In order to require reconstructed electrons to only be reconstructed from real electrons, the setting Author = 1 is used. Electrons are also required to have pseudorapidities of $|\eta| < 2.47$ with the exception of $1.37 < |\eta| < 1.52$ due to the transition region between the barrel and the end-caps in the LAr calorimeter. The aforementioned selection is summarized in Table 4.

Table 4: Selection for identified electrons.

p_{T} range	Electron ID	η range	Author	Impact parameter
< 25 GeV	LHTight	$\|\eta\|$ <1.37, $1.52 < \eta < 2.47$	1	$\|z_0 \sin\theta\| < 0.5$ mm, $\frac{\|d_0\|}{\sigma(d_0)} < 5$
> 25 GeV	LHMedium	$\|\eta\|$ <1.37, $1.52 < \eta < 2.47$	1	$\|z_0 \sin\theta\| < 0.5$ mm, $\frac{\|d_0\|}{\sigma(d_0)} < 5$

5.3 Muons

Muons are reconstructed using mostly information from the inner detector and the Muon Spectrometer, although the calorimeters are also used to some extent. Ref. [43] provides a detailed description of how the reconstruction is conducted. Muon candidates are categorized as either *Loose*, *Medium* or *Tight* based on the quality of the reconstruction and only Tight quality muons are considered in this analysis. Selected muons are required to be within the pseudorapidity range of $|\eta| < 2.5$. The muon selection is summarized in Table 5.

Table 5: Selection for identified muons.

p_{T} range	Muon ID	η range	Impact parameter
> 15 GeV	Tight	$\|\eta\| < 2.5$	$\|z_0 \sin\theta\| < 0.5$ mm, $\frac{\|d_0\|}{\sigma(d_0)} < 3$

5.4 Jets

Because of the effects of color confinement, quarks and gluons produced in collisions rapidly hadronize. A shower of hadrons then continues to travel in the same direction as the original parton due to the conservation of momentum, producing multiple energy deposits in the calorimeters. Because of the abundance of quarks and gluons in any given

collision, it is advantageous to consider such a collection of particles a single object called a jet. The complexity arising from measurements of jets makes the definition of a jet exceedingly important.

The anti-k_t algorithm [44] is used to construct jets in this analysis with a radius parameter of $R = 0.4$, implemented using the FastJet package [45]. Collections of positive energy topo-clusters remaining after the energy subtraction step of the Particle Flow algorithm are used as inputs to FastJet. The details of this process are beyond the scope of this thesis, but are thoroughly explained in Ref. [46]. All jets are required to be in the range of $|\eta| < 4.5$ and have a transverse momentum of $p_{\mathrm{T}} > 20$ GeV. EMPFlow jets between $20 < p_{\mathrm{T}} < 60$ GeV are required to pass JVT > 0.5 where JVT is the *Jet Vertex Tagger* [47]. Jets in the range $20 < p_{\mathrm{T}} < 30$ GeV are considered "sub-threshold" and are used in the counting of b-tagged jets (see section 5.5) while jets with $p_{\mathrm{T}} > 30$ GeV are included in the jet counting.

5.5 b-tagged jets

Events containing b-hadrons are of major interest as $h \to b\bar{b}$ is the primary decay channel with the largest BR of the Higgs boson [48]. Reconstructed jets originating from a b quark are therefore tagged and referred to as *b-tagged jets* or simply b-jets. The DL1r b-tagging algorithm [1], which is a deep-learning neural network, is used to identify jets containing b-hadrons. Jets originating from b-quarks must have $p_{\mathrm{T}} > 20$ GeV and be within the region $|\eta| < 2.5$ to be considered b-jets. b-jets are also selected to have at least 85% efficiency, determined by simulated $t\bar{t}$ events.

5.6 Pre-selection

In addition to the above mentioned conditions, a set of event pre-selection requirements are applied. Standard cuts on the overlap [50] of $V\gamma$ and Vjets, as well as jet cleaning [51] are applied. Trigger selection and trigger matching are also applied, and are described in Ref [52]. Exactly two leptons are selected to have different flavor and opposite charge, giving the possible combinations $e^+\mu^-$ and $e^-\mu^+$. The leading lepton, meaning that it is the lepton with highest p_{T}, is required to have a transverse momentum $p_{\mathrm{T}} > 22$ GeV while the sub-leading lepton is required to have $p_{\mathrm{T}} > 15$ GeV. As some processes already

[1] The DL1r algorithm is an update of the DL1 algorithm [49]. No official documents on the DL1r algorithm has been published as of writing this thesis.

have a threshold on the dilepton invariant mass m_{ll}, a requirement on all leptons to have $m_{ll} > 10$ GeV is used for consistency.

6 Main Analysis Optimization

In order to maximize the signal yields while at the same time minimizing the background yields, a main event selection can be constructed. The relative strength of signal yields with respect to the background varies for different threshold requirements applied on the kinematic variables. Setting up a selection that rejects regions of a kinematic variable that is rich in background yields therefore enhances the signal efficiency. The kinematic variables of interest in this analysis are

- Transverse momentum of the leptons, p_{T}^{ll}
- Invariant mass, m_{ll}
- Transverse mass, m_{T}
- Missing transverse energy, E_{T}^{miss}
- Angular separation between leptons, ΔR_{ll}
- Difference in azimuthal angle, $\Delta\phi_{ll}$
- Difference in pseudorapidity, $\Delta\eta_{ll}$
- Number of b-jets, n_{bjet}.

The construction of the event selection is discussed in Section 6.2.

An effective method to evaluate the signal yield with respect to the background is to calculate the *significance*. There exists a variety of definitions, and the choice depends on the analysis. In this analysis, the approximate Poisson significance is used as the default definition if nothing else is stated. It is defined as

$$\sigma_p = \sqrt{2((s+b)\log(1+s/b)-s)} \tag{6}$$

where s is the signal yield and b is the background yield. The Poisson significance is a solid general purpose definition although sometimes too general, making it necessary to introduce complementary definitions.

As will be investigated in Section 6.1, the choice of isolation is important in order to minimize the amount of misidentified leptons. Due to misidentified leptons originating mainly from W+jets processes, an additional significance definition introduced in the 2020 $H \to WW^*$ optimization note [53] that takes the uncertainty of W+jets into account is

used. It is defined as

$$\sigma_{W+\text{jets}} = \frac{s}{\sqrt{s + b + \delta^2_{W+\text{jets bkg}} + \delta^2_{\text{Other bkg}}}}, \tag{7}$$

where $\delta^2_{W+\text{jets bkg}}$ is the uncertainty in W+jets background and $\delta^2_{\text{Other bkg}}$ is the uncertainty in the total background excluding W+jets. As in the $H \to WW^*$ optimization note, $\delta^2_{W+\text{jets bkg}}$ and $\delta^2_{\text{Other bkg}}$ are set to 40% and 10% respectively, as they represent conservative estimates of the total systematic uncertainty affecting each process. This definition is necessary as W+jets has a relatively small background contribution compared to the total background. Using different isolation working points therefore only has minor effect on the Poisson significance, as it only takes the total signal and background yields into account. The $H \to WW^*$ definition is significantly more sensitive to different isolation working points, and is used to select the best performing working point.

6.1 Optimization of Isolation Working Points

During the reconstruction of objects in the detector, it is not impossible that other particles are misidentified as leptons. Although muons run a low chance of being misidentified due to being unique in fully penetrating the calorimeter, electrons have a relatively high chance. This is due to there being numerous other particles such as charged hadrons that leave curved tracks and deposit their energy in the EM calorimeter [54]. Correctly identified leptons originate from hard interactions or decays of unstable states, such as final-state radiation or mesons. Leptons that do not stem from hard interactions tend to be surrounded by other particles and energy deposits, thus creating a distinguishable feature of misidentified leptons. It is then possible to create isolation variables which can be used to differentiate between prompt and non-prompt leptons. They are defined as the ratio of the sum of the energy or momentum in a cone around the lepton, and the p_{T} of the lepton. The smaller the ratio, the larger the probability of the lepton being prompt due to being more isolated.

There exists a variety of isolation working points [55] that are provided by the Isolation and Fake Forum Group (IFF). Due to the difference in the reconstruction of electrons and muons, some isolation working points are defined differently for each lepton. The isolation working points considered in this analysis can all be found in Ref. [56] and are listed in Table 6.

Table 6: All isolation working points that were evaluated in this analysis and their designated lepton flavor.

Lepton	Isolation Working Point
Electron	FCHighPtCaloOnly TightLoose
Muon	FixedCutHighPtTrackOnly FCTightTrackOnly FCTightTrackOnly_FixedRad
Both	FCTight FCLoose FCTight_FixedRad FCLoose_FixedRad FixedCutPflowLoose PromptLeptonVeto

6.1.1 Initial Selection

Before evaluating the highest performing isolation working point for this analysis, an initial selection was performed. All isolation working points follow standard definition with the exception of TightLoose, which is defined as FCTight when $p_{\mathrm{T}} < 25$ GeV and FCLoose otherwise. The preselection described in Section 5 was used with a cut on $p_{\mathrm{T}} > 30$ GeV, and a region of $m_{ll} < 150$ GeV was constructed due to signal yields being negligible at $m_{ll} > 150$ GeV. In order to gain further insight into the performance of the isolation working points, the m_{ll} region was further divided into three sub-regions: $0 < m_{ll} < 50$ GeV, $50 < m_{ll} < 100$ GeV and $100 < m_{ll} < 150$ GeV. As can be seen in Figure 11, the majority of the signal yields are concentrated in the lower m_{ll} regions, making the choice of the optimal isolation working point increasingly driven by such regions. Each isolation working point is evaluated for each signal mass points, based on the W+jets significance in each m_{ll} region. The highest performing isolation working points are found to be FCTight, FCLoose and FCTightTrackOnly.

6.1.2 Selection of Isolation Working Point

In order to evaluate the highest performing isolation working points, they are applied separately for each lepton such that every combination was tested. The possible combinations and their notations are listed in Table 7. Note that the working point FCTightTrackOnly is defined for muons only which limits the total number of combinations to six. The same selection as for the initial selection of isolation working points was used, as well as the

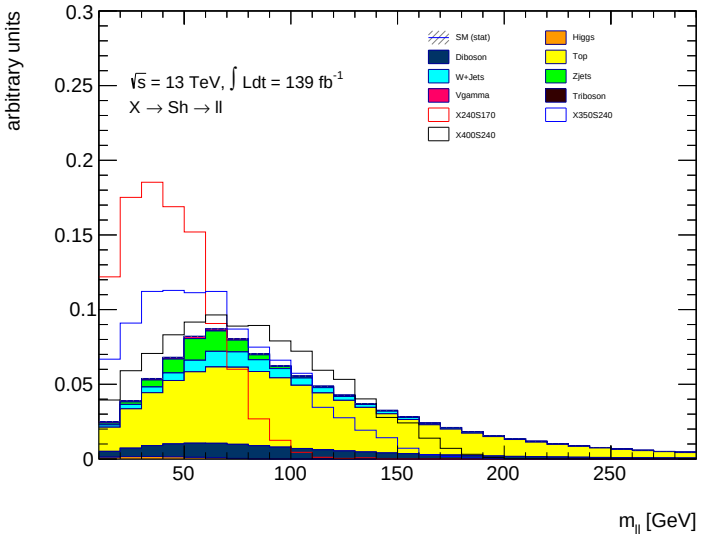

Figure 11: Kinematic distribution of the dilepton invariant mass, normalized to unity. The fully colored distributions correspond to yields of different background processes while the empty distributions correspond to the yields of the signal mass points.

three regions of m_{ll}.

Table 7: The possible combinations of isolation working points for each lepton flavor.

Electron	Muon	Notation
FCTight	FCTight	eTight_mTight
FCTight	FCLoose	eTight_mLoose
FCLoose	FCTight	eLoose_mTight
FCLoose	FCLoose	eLoose_mLoose
FCTight	FCTightTrackOnly	eTight_mTightTrackOnly
FCLoose	FCTightTrackOnly	eLoose_mTightTrackOnly

There are some differences in dynamics depending whether the electron or the muon is the leading lepton. One important difference is that the contribution from misidentified leptons are higher for electrons, which makes a noticeable difference if the leading lepton is an electron. The event yields are therefore split into two channels: $e\mu$ and μe, where $e\mu$ denotes that the electron is the leading lepton and vice versa.

Tables 20 and 21 in Appendix A show the full event yields for the signal, total background and W+jets for the selection of isolation working points in the $e\mu$ and μe channel respectively. The significance was calculated using Equation 7 for every combination of isolation working point, in each m_{ll} range for every signal mass point. Figures 12 and 13 show the significances in the $e\mu$ and μe channel respectively where the uncertainties are purely statistical. The larger uncertainties in the $X240S170$ mass point significances is

a result of signal yields being relatively small compared to the other signal mass points, giving poorer statistics. As can be seen in Figure 11, the $X240S170$ signal yields (indicated by the red line) are negligible in the $100 < m_{ll} < 150$ GeV region, and are omitted from the significance calculation due to giving trivial results. Figures 12 and 13 show that using the eTight_mTight working point meaning FCTight for both the electron and muon gives the highest significance for all signal mass points and m_{ll} ranges, in both channels. This is in line with the choice of isolation working point in the $H \to WW^*$ analysis [41], and is the choice of isolation in the following sections of this analysis.

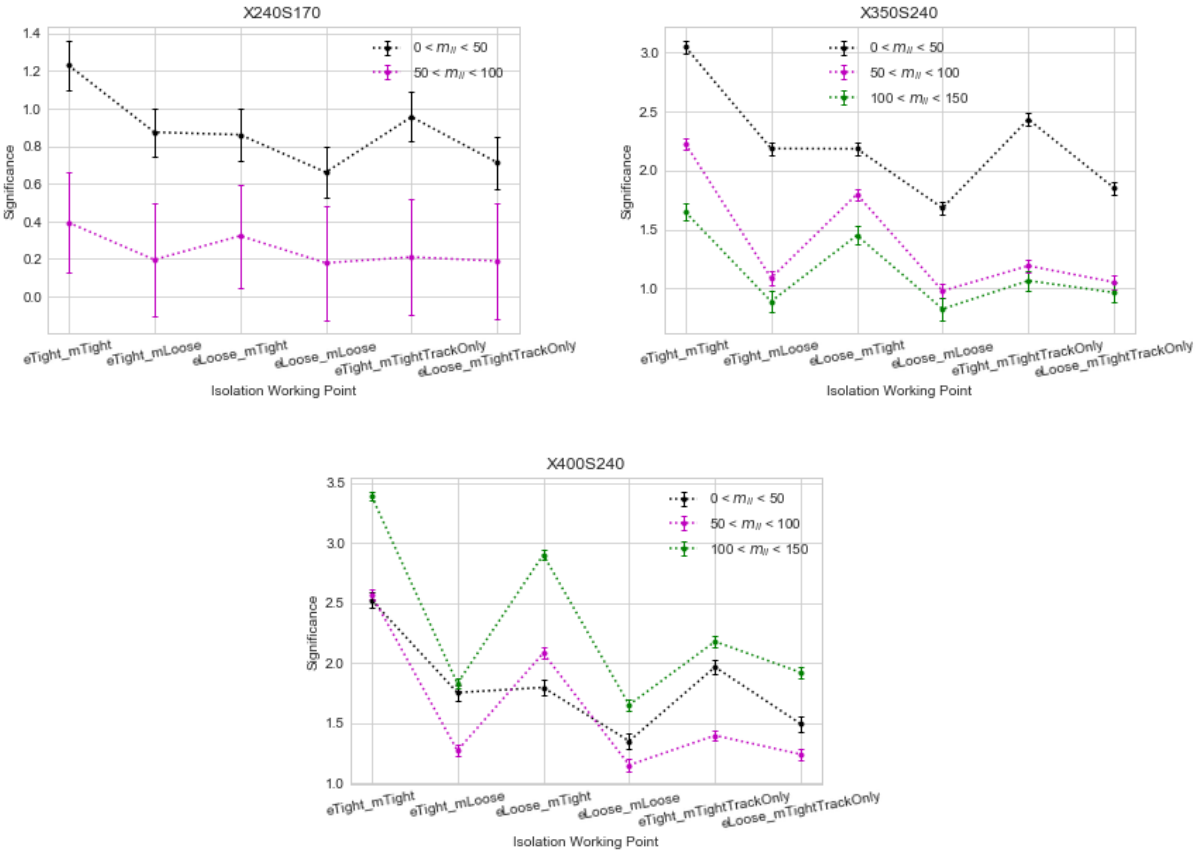

Figure 12: The signal significance from Eq. 7 of each isolation working point for each mass point in the $e\mu$ channel.

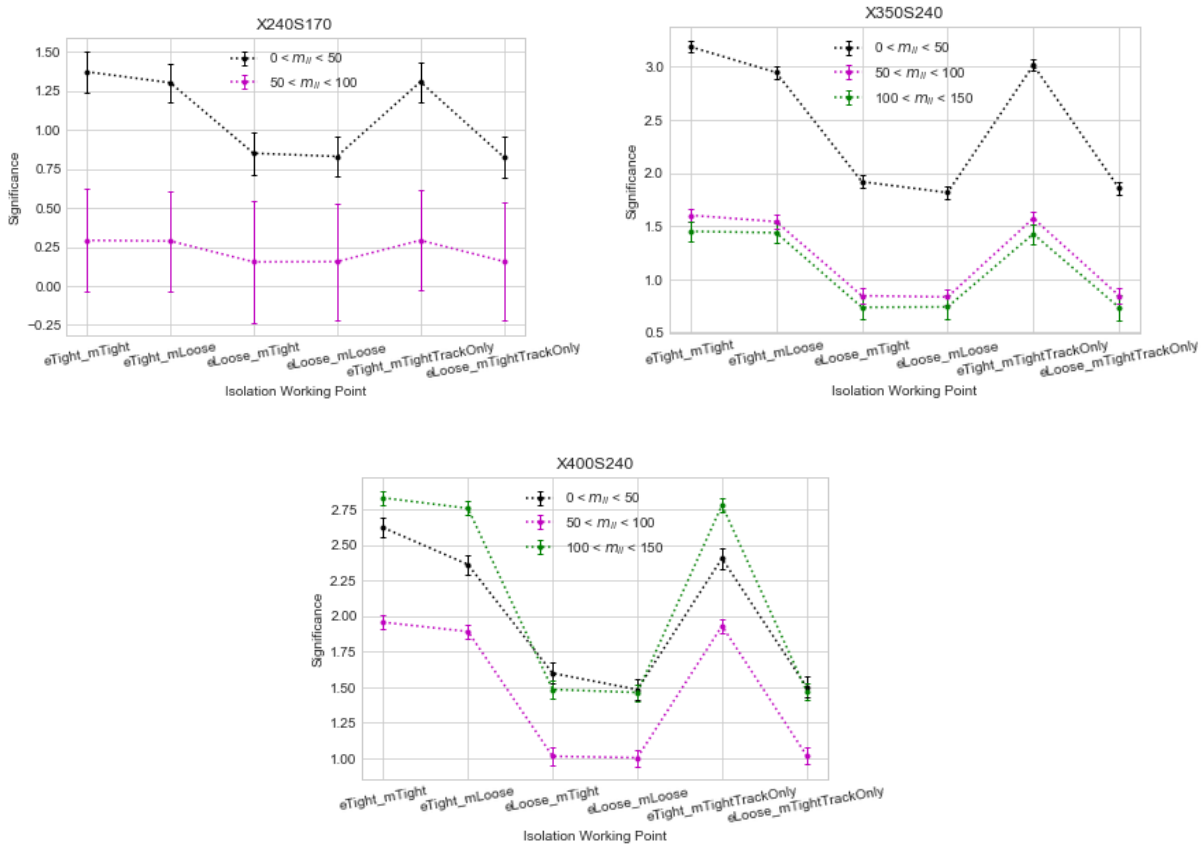

Figure 13: The signal significance from Eq. 7 of each isolation working point for each mass point in the μe channel.

6.2 Event Selection

The event selection is constructed by performing a scan on the significance for each main kinematic variable (see Section 6). The kinematic variables are correlated of varying degree, and it is important to take that into account when performing a significance scan. Scanning the significance separately for each kinematic variable would ignore their interdependency, making a multidimensional significance scan advantageous.

Before conducting a scan, histograms for each kinematic variable are defined. A cut is then applied on a bin for each kinematic variable and the total Poisson significance is evaluated. A new cut is then applied on the next bin for one of the kinematic variables, and the significance is evaluated again. The process is repeated such that the scan is performed by evaluating the significance for every combination of cuts, for each signal mass point. The combination of cuts that give the highest significance out of all possible combination should in principle be the optimal choice of cuts for the analysis region. A multidimensional scan can be very computationally heavy due to scaling significantly with the number of kinematic variables as well as the number of bins per variable. It is

therefore necessary to reduce the number of inputs by making a few assumptions.

An initial assumption is that optimal threshold values found by using multidimensional scanning are in the relative vicinity of optimal cuts found by scanning each kinematic variable independently. This allows for the reduction of the scanning range and thus the number of bins of each kinematic variable when using multidimensional scanning, reducing the number of iterations of the algorithm drastically. This method is used conservatively in order to not risk disregarding optimal cuts. Figure 14 shows normalized kinematic distributions with the signal yields of the X240S170 mass point in the $e\mu + \mu e$ channel, along with a significance scan. Figures 19 and 20 in Appendix B show the kinematic distribution for the other signal mass points. The $e\mu + \mu e$ channel is the combination of the $e\mu$ and μe channels, where the yields are added together. The blue line in the significance scan denotes the significance if an upper cut is applied, rejecting all events above that threshold. The red line denotes the significance if a lower cut is applied. The choice of lower or upper cut is dependent on which cut preserves most of the signal yields while rejecting the most background.

In order to further decrease the computational time, the number of dimensions in the multidimensional scan is reduced by making a few assumptions. A cut on $n_{b\text{jets}} < 2$ is assumed as events with two or more b-jets contain only $\sim 10\%$ of the total signal, and are mostly dominated by the $t\bar{t}$ process. A cut on $m_{ll} < 150$ GeV is also assumed for the same reason. Table 8 shows the optimal cuts determined by performing a multidimensional significance scan for each signal mass point. As the signal is concentrated to higher regions for a majority of the kinematic variables for the higher-mass signal mass points, the optimal threshold value also increases. The only exception is E_{T}^{miss}, where no cut was found that gave an increase in significance. The same pattern is seen in m_{T} for the $X400S240$ mass point, where a lower cut gives better significance due to the signal being concentrated to higher regions.

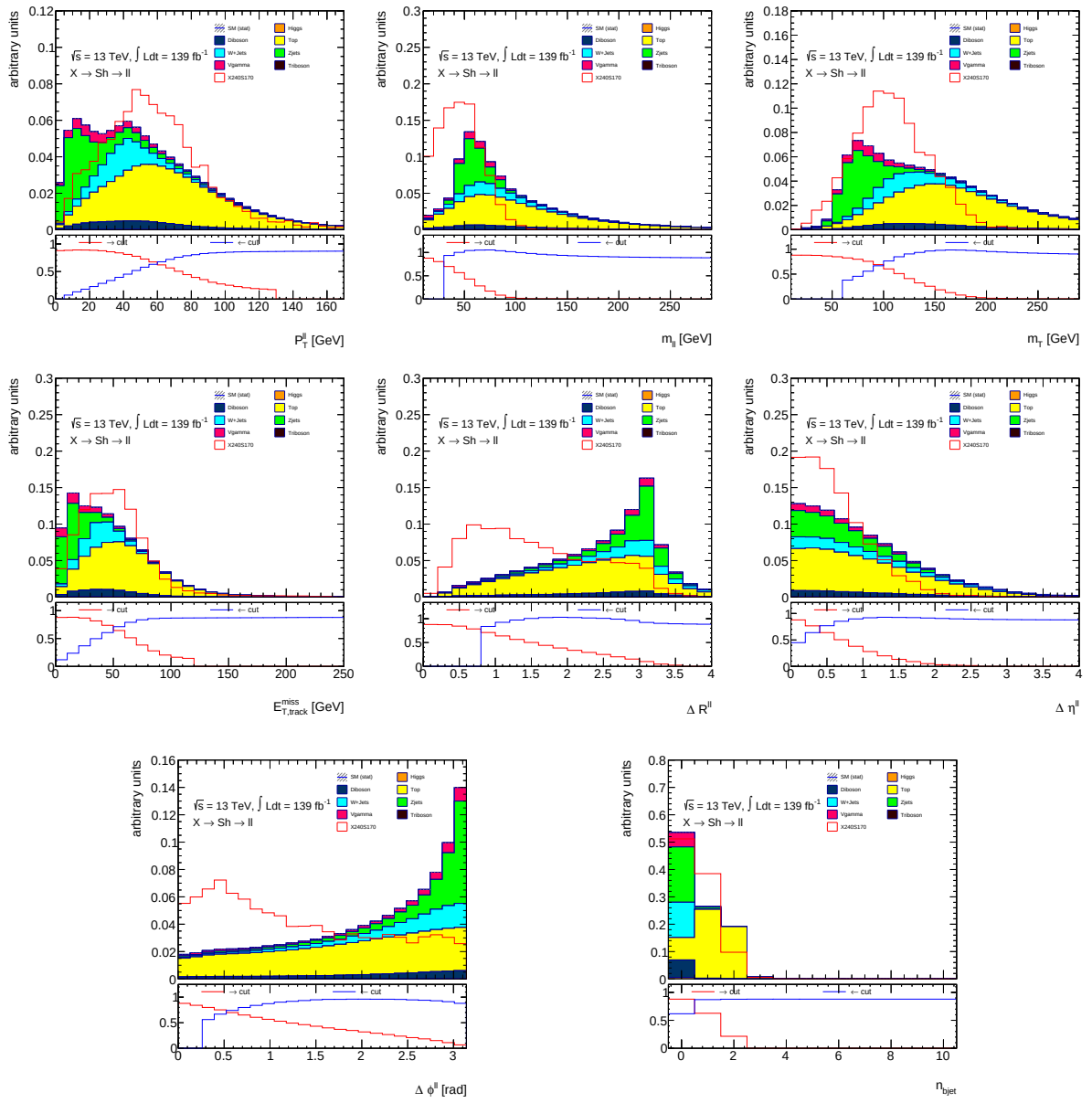

Figure 14: Normalized kinematic distributions in the $e\mu + \mu e$ channel where the signal yields correspond to the X240S170 mass point.

Table 8: The best obtained cuts determined by performing a multidimensional significance scan for each mass point.

$X240S170$	$X350S240$	$X400S240$
$p_{\mathrm{T}}^{ll} > 25.5$ GeV	$p_{\mathrm{T}}^{ll} > 34$ GeV	$p_{\mathrm{T}}^{ll} > 34$ GeV
$m_{\mathrm{T}} < 184$ GeV	$m_{\mathrm{T}} < 242$ GeV	$m_{\mathrm{T}} > 10$ GeV
$E_{\mathrm{T}}^{miss} > 0$ GeV	$E_{\mathrm{T}}^{miss} > 0$ GeV	$E_{\mathrm{T}}^{miss} > 0$ GeV
$\Delta R_{ll} < 1.7$	$\Delta R_{ll} < 2.6$	$\Delta R_{ll} < 3.2$
$\Delta\phi_{ll} < 1.7$ rad	$\Delta\phi_{ll} < 2.5$ rad	$\Delta\phi_{ll} < 2.8$ rad
$\Delta\eta_{ll} < 1.5$	$\Delta\eta_{ll} < 1.8$	$\Delta\eta_{ll} < 2.2$

Because the interdependency of the kinematic variables vary, some contribute heavily in the evaluation of significance while others have insignificant effect. The significance can be re-evaluated using the best-obtained cuts in Table 8 while removing one or multiple cuts. If the change in total significance is minor when disregarding certain cuts, they can safely be omitted from the event selection in order to have a straightforward selection while preserving high significance. The upper section of Table 9 shows the change in significance when removing one cut at a time for each signal mass point. The cuts that had the least effect on the significance when removed were the cuts on $\Delta\phi_{ll}$, ΔR_{ll} and p_{T}^{ll}. This is due to the variables being correlated, and applying the cuts would mainly attempt to remove the same Z+jets background (see Figure 14). Another evaluation of the significance was performed while removing combinations of cuts on $\Delta\phi_{ll}$, ΔR_{ll} and p_{T}^{ll} and the resulting change in significance can be seen in the lower section of Table 9. Removing the cuts on p_{T}^{ll} and ΔR_{ll} had the least impact on the significance on average across all three signal mass points, and were subsequently omitted from the event selection.

Table 9: The changes in the significance when cuts on each kinematic variable for each signal mass point. The uncertainties are purely statistical.

Removed cut	Sign. ($X240S170$)	Sign. ($X350S240$)	Sign. ($X400S240$)
None	0.437 ± 0.011	1.384 ± 0.021	1.541 ± 0.022
p_{T}^{ll}	0.437 ± 0.011	1.370 ± 0.020	1.501 ± 0.021
m_{T}	0.422 ± 0.010	1.372 ± 0.020	1.541 ± 0.022
ΔR_{ll}	0.431 ± 0.010	1.377 ± 0.021	1.539 ± 0.022
$\Delta\phi_{ll}$	0.437 ± 0.011	1.383 ± 0.021	1.533 ± 0.022
$\Delta\eta_{ll}$	0.435 ± 0.010	1.377 ± 0.021	1.536 ± 0.022
p_{T}^{ll}, ΔR_{ll}, $\Delta\phi_{ll}$	0.338 ± 0.005	1.204 ± 0.005	1.375 ± 0.004
p_{T}^{ll}, $\Delta\phi_{ll}$	0.326 ± 0.010	1.368 ± 0.006	1.410 ± 0.005
p_{T}^{ll}, ΔR_{ll}	0.432 ± 0.010	1.361 ± 0.007	1.497 ± 0.006
ΔR_{ll}, $\Delta\phi_{ll}$	0.377 ± 0.007	1.337 ± 0.006	1.527 ± 0.006

The final step in constructing the event selection is to determine a single selection for all three signal mass points. In order to preserve high significance for all three signal mass points, cuts that preserve most of the signal yields across all signal mass points are used. For example, if the optimal cuts for the $X400S240$ were to be used, a significant portion of the signal would be rejected for the lower signal mass points. The remaining cuts on m_{T}, $\Delta\phi_{ll}$ and $\Delta\eta_{ll}$ for the $X240S170$ mass point are therefore used as baseline. The cuts can then be varied slightly, and the significance can be evaluated for all three signal mass points. The selection that gives the best overall significance across all signal mass points is

- Invariant mass, $m_{ll} < 150$ GeV
- Transverse mass, $m_{\mathrm{T}} < 260$ GeV
- Difference in azimuthal angle, $\Delta\phi_{ll} < 2.7$
- Difference in pseudorapidity, $\Delta\eta_{ll} < 1.5$
- Number of b-jets, $n_{b\mathrm{jet}} < 2$.

Table 10 presents the full event selection with the signal yields and significance for each signal mass point, and the total background yields in the $e\mu+\mu e$ channel. The significance shows an increase for all three signal mass points as a result of the event selection.

Table 10: Cutflow of the full event selection with signal yields and significance in the $e\mu + \mu e$ channel.

	X240S170	**X350S240**	**X400S240**	**X240S170 Sig**	**X350S240 Sig**	**X400S240 Sig**	**Total Background**
Channel Selection	9201.24 ± 104.10	35152.19 ± 273.02	42452.17 ± 315.78	3.37 ± 0.04	12.87 ± 0.10	15.54 ± 0.12	7444296.64 ± 6564.74
Trigger Selection	8428.33 ± 99.69	33662.27 ± 267.33	40954.84 ± 310.24	3.21 ± 0.04	12.79 ± 0.10	15.56 ± 0.12	6911638.14 ± 6251.94
Trigger Matching	7756.37 ± 94.35	31676.75 ± 256.85	38591.81 ± 298.62	3.11 ± 0.04	12.69 ± 0.10	15.45 ± 0.12	6224286.50 ± 5689.15
Overlap: Vgamma/Vjets	7756.37 ± 94.35	31676.75 ± 256.85	38591.81 ± 298.62	3.19 ± 0.04	13.00 ± 0.11	15.83 ± 0.12	5927598.71 ± 5384.60
$p_t^{lead} > 22$ GeV	7756.37 ± 94.35	31676.75 ± 256.85	38591.81 ± 298.62	3.19 ± 0.04	13.00 ± 0.11	15.83 ± 0.12	5927598.71 ± 5384.60
$p_t^{sublead} > 15$	6161.75 ± 84.12	27256.13 ± 238.75	33503.00 ± 278.77	3.16 ± 0.04	13.96 ± 0.12	17.16 ± 0.14	3800804.06 ± 3398.00
$m_{\ell\ell} > 10$ GeV	5962.69 ± 82.76	26863.64 ± 237.03	33111.81 ± 277.15	3.10 ± 0.04	13.96 ± 0.12	17.21 ± 0.14	3692720.64 ± 3275.52
OS Leptons	5086.98 ± 76.42	20447.73 ± 206.76	24322.94 ± 237.54	2.86 ± 0.04	11.48 ± 0.12	13.65 ± 0.13	3164945.61 ± 2652.26
DL1r: $N_{b\text{-}jet} \leq 1$	4560.50 ± 72.45	17561.70 ± 191.95	20871.37 ± 220.21	2.86 ± 0.05	11.02 ± 0.12	13.09 ± 0.14	2533465.54 ± 2646.89
$m_{\ell\ell} < 150$ GeV	4554.36 ± 72.40	17297.63 ± 190.51	19908.90 ± 214.89	3.09 ± 0.05	11.73 ± 0.13	13.50 ± 0.15	2167362.38 ± 2526.25
$\Delta\eta_{\ell\ell} < 1.5$	4321.55 ± 70.59	15656.67 ± 181.44	17498.64 ± 201.67	3.22 ± 0.05	11.66 ± 0.14	13.03 ± 0.15	1796573.65 ± 2219.68
$m_T < 260$ GeV	4320.36 ± 70.58	15594.85 ± 181.07	17348.01 ± 200.80	3.24 ± 0.05	11.69 ± 0.14	13.00 ± 0.15	1773954.65 ± 2216.69
$\Delta\varphi_{\ell\ell} < 2.7$[rad]	3930.06 ± 67.33	13791.84 ± 170.26	15041.36 ± 186.83	3.75 ± 0.06	13.15 ± 0.16	14.33 ± 0.18	1096156.59 ± 1658.73

7 The Fake Factor Method

Although the ATLAS detector exhibits high efficiencies in the reconstruction of events, it is not flawless. Dilepton decays originating from W bosons can occasionally be difficult to distinguish from non-prompt leptons, resulting in jets and other particles sometimes being misidentified as leptons. These fake leptons are simply referred to as "fakes". The rate of misidentification is challenging to accurately model using MC simulation and needs to be accounted for in other ways. In this analysis, W+jets is a large contributor to the background and thus a major source of fakes. The *fake factor* method is a data-driven technique that estimates the amount of misidentification efficiently, and will be described in this chapter.

7.1 Origin of Fakes

The ATLAS detector provides excellent lepton identification which in general leads to accurate background suppression. Only a small amount of jets get misidentified, but due to standard W processes having high cross sections compared to signal processes they need to be accounted for accurately. The misidentification of leptons can come from a variety of sources depending on the lepton flavor [57]. Electron fakes can arise from charged hadrons, semi-leptonic heavy-flavor decays and photon conversions. In the latter two cases, real electrons are included in the final state although they are still considered fake. Only the leptons produced from the decay of W bosons are considered real leptons, and are referred to as prompt leptons. Muon fakes originate from semi-leptonic heavy flavor decays or meson decays. In the case of both flavors, fake contribution is higher for lower p_{T}.

There are multiple reasons why the rate of fakes is not accounted for in the MC simulation. In order to accurately predict the fake contribution, simulations of all misidentified particles as well as the rate of misidentification would be required. The modeling of the rates would also require accurate modeling of non-Gaussian tails of the detector response to the jets. The sources of all fake leptons would also have to be predicted. Taking all these factors into account would require significantly higher levels of detail in the MC, making the fake factor method a more suitable choice [57].

7.2 Fake Factor Method

The idea of the fake factor method is to select a control sample that is enriched in the background being estimated, and use an extrapolation factor to relate those events to the background in the main analysis. This extrapolation factor is what is known as the fake factor. The control region is defined to select the background that is being estimated in a way that increases the rate of misidentification. The number of fake leptons is estimated by constructing a region where leptons that do not meet lepton identification criteria still satisfy looser requirements designated for fakes. The tighter criterion is called identified (ID) and is the same as described in Section 5. The looser criterion is called anti-identified (anti-ID). The ID and anti-ID lepton requirements are listed in Tables 11 and 12 for electrons and muons respectively. The fake factor relates the number of fake leptons that pass the full ID selection, to the number of fake leptons that pass the anti-ID selection. Because of the different properties of electrons and muons, the fake factor is measured separately.

An assumption of the fake factor method is that the efficiency of fake leptons depends on the properties of the lepton, and not of the rest of the event. This is justified as lepton reconstruction uses information from a small region of the detector [41]. The estimation of the fake factor can thus be done in a three-lepton selection in a Z+jets enriched region where two prompt leptons originate from a Z boson and the third lepton is a fake candidate. The fake factor is calculated using

$$F = \frac{N^{data}_{i,i,i} - N^{\text{non-}Z\text{+Jets(MC)}}_{i,i,i}}{N^{data}_{i,i,a} - N^{\text{non-}Z\text{+Jets(MC)}}_{i,i,a}}. \tag{8}$$

The subscripts i and a denote if the lepton is ID or anti-ID respectively. The superscript *data* denotes that the yield N is measured from p-p collisions, while the superscript non-Z+Jets(MC) means that the yield comes from all MC simulation processes excluding Z+jets contribution. The fake factor can then be applied to the W+jets process, using the expression

$$N^{W\text{+jets}}_{\text{ID+ID}} = F \times N^{W\text{+jets}}_{\text{ID+anti-ID}}, \tag{9}$$

where $N^{W\text{+jets}}_{\text{ID+ID}}$ is the yield in a region where both leptons pass ID, and $N^{W\text{+jets}}_{\text{ID+anti-ID}}$ is the yield with one ID and one anti-ID lepton.

Table 11: Selection criteria for ID and anti-ID electrons.

ID	Both	anti-ID
Pass LHTight if $p_t < 25$ GeV Pass LHMedium if $p_T > 25$ GeV Pass FCTight Isolation	$p_{\mathrm{T}} > 15$ GeV $\lvert\eta\rvert$ <2.47, excluding $1.37 < \lvert\eta\rvert < 1.52$ $\lvert z_0 \sin\theta\rvert < 0.5$ mm $\lvert d_0\rvert/\sigma(d_0) < 5$ Author = 1	Pass LHLoose Fail FCTight Isolation

Table 12: Selection criteria for ID and anti-ID muons.

ID	Both	anti-ID
$\lvert d_0\rvert/\sigma(d_0) < 3$ Pass Quality Tight Pass FCTight Isolation	$p_{\mathrm{T}} > 15$ GeV $\lvert\eta\rvert < 2.5$ $\lvert z_0 \sin\theta\rvert < 0.5$ mm	$\lvert d0\rvert/\sigma(d_0) < 15$ Pass Quality Medium Fail FCTight Isolation

7.3 Z+jets Control Region

In order to calculate the fake factor, a region which is enhanced in Z+jets is defined. Events with three lepton candidates with a total charge of ± 1 are considered where all leptons are required to have $p_{\mathrm{T}} > 15$ GeV. The selection is split into four different categories based on the possible flavor combinations: three muons, two muons and an electron, two electrons and one muon, and three electrons. The selection of leptons is done in such a way where the leading lepton (l_0) has different charge than the other leptons (l_1 and l_2). This means that in principle l_0 can not be a fake as it originates from a Z boson decay along with l_1 or l_2. This leaves l_1 and l_2 as the only possible fake candidates. Because of this, there are eight distinct combinations where a fake candidate can be identified. Table 13 highlights the different categories and their notations. The flavor of the fake candidate is also highlighted as it is dependent on the lepton combination. For example, if the flavor combination is two muons and an electron, the two muons originate from a Z boson leaving the electron as a fake candidate.

Table 13: Different combinations of leptons and fake candidates in the Z+jets analysis region. The fake lepton flavor denotes the flavor of the fake in each respective combination of leptons.

Lepton Combination	Fake Candidate	Fake Candidate Flavor	Notation
Muon, Muon, Muon	l_1	Muon	mmml1
Muon, Muon, Muon	l_2	Muon	mmml2
Electron, Muon, Muon	l_1	Electron	emml1
Electron, Muon, Muon	l_2	Electron	emml2
Electron, Electron, Muon	l_1	Muon	eeml1
Electron, Electron, Muon	l_2	Muon	eeml2
Electron, Electron, Electron	l_1	Electron	eeel1
Electron, Electron, Electron	l_2	Electron	eeel2

In order for two leptons to qualify as Z decay particles, they need to be of the same flavor and of opposite charge and have an invariant mass between [80, 110] GeV if they are electrons, and [70, 110] GeV if they are muons. If both combinations of l_0, l_1 and l_0, l_2 pass these criteria, the pair closest to the mass of the Z boson is considered Z decay leptons and the remaining lepton is considered a fake candidate. A cut on the $m_{\mathrm{T}} < 50$ GeV is applied in order to reduce events with leptonic WZ decays. The Z decay leptons both need to pass the ID criteria. Two regions are then constructed depending on whether the fake candidate passes ID or anti-ID. The full cutflows can be found in Tables 22 and 23 in Appendix A.

The WZ process contributes largely to the total background in the Z+jets region and is a major component in the uncertainty of the fake factor. A WZ control region (CR) is therefore constructed by reversing the cut on the transverse mass to be $m_T > 50$ GeV. This region is very pure in WZ, and a combined normalization factor $((N^{\text{data}} - N^{\text{non-}WZ,\text{MC}})/N^{WZ,\text{MC}})$ using all eight categories was calculated to be 1.00 ± 0.01. The normalization factor for each category is presented in Table 14.

Table 14: Normalization factors for the different fake candidate categories in the WZ CR. The uncertainties are statistical.

Category	Normalization Factor
mmml1	1.01 ± 0.01
mmml2	0.98 ± 0.01
eeml1	1.02 ± 0.01
eeml2	0.93 ± 0.01
eeel1	1.01 ± 0.01
eeel2	1.00 ± 0.01
emml1	1.01 ± 0.01
emml2	1.06 ± 0.01

7.4 Electroweak Uncertainty

The fake factor that is obtained using Equation 8 relies on non-Z+jets processes which can have theoretical uncertainties in the normalization, resulting in systematic uncertainty in the fake factor. This is referred to as electroweak subtraction uncertainty. The anti-ID regions are mainly populated by fakes while the ID regions contain mostly electroweak background processes. This means that the calculation of the fake factor is predominantly sensitive to MC uncertainties in the ID region and influenced negligibly in the anti-ID region. The uncertainties in the anti-ID region can therefore be neglected.

As can be seen in the cutflows in Tables 22 and 23 in Appendix A, the dominant contribution to the background comes from the WZ process. The uncertainty estimation is therefore approximated to have WZ as the only contributor. The WZ yield is dependent on the normalization factors in the WZ CR, and thus the uncertainties need to be extrapolated from the WZ CR to the Z+jets CR. This is done by taking the difference in the normalization factor between the largest varying categories in the WZ CR (see Table 14), giving a variation of 13%. The WZ normalization in the Z+jets CR can then be varied by that amount to obtain an estimate of the uncertainty in the fake factors.

7.5 Fake Factor Computation

The fake factors were calculated using Equation 8 for each fake candidate category and are presented in Table 24 in Appendix C. The total fake factors for the electron and muon were also calculated by combining the yields of the different categories for each respective lepton and are presented in Table 15. The uncertainties in Table 24 are purely statistical

while the uncertainties in Table 15 are the combined statistical and electroweak uncertainty. The majority of the uncertainty in the fake factors emerge from the electroweak contribution, and the muon is significantly more affected. This can mostly be attributed to WZ processes having relatively higher yields compared to the total background for events including fake muons than for events including fake electrons (see Table 22 and 23).

Table 15: Fake factors for the electron and muon with statistical and electroweak uncertainty.

Lepton Flavor	Fake Factor
Electron	0.127 ± 0.023
Muon	0.041 ± 0.024

7.6 Same Sign Control Region

In order to validate the accuracy of the fake factor method, the fake factors are evaluated in a region enriched in the W+jets process. The same preselection as described in Section 6.2 is used, with the exception of selecting for same sign instead of opposite sign leptons. To suppress the signal yields to be within the statistical uncertainties of the total background yield, a cut on $\Delta\phi_{ll}$ is made. Figure 15 shows the distributions of $\Delta\phi_{ll}$ where the signal yield are concentrated primarily to $\Delta\phi_{ll} < 2.0$ and thus a cut on $\Delta\phi_{ll} > 2.0$ is applied. Figure 16 shows a direct comparison between two p_T distributions with and without the implementation of the fake factor. Figure 17 presents distributions of the main kinematics in the same sign CR. The kinematic distributions without the application of fake factors can be seen in Figure 21 in Appendix B. It is clear from the figures that the application of the fake factor method provides a more accurate W+jets estimation than using purely MC simulation.

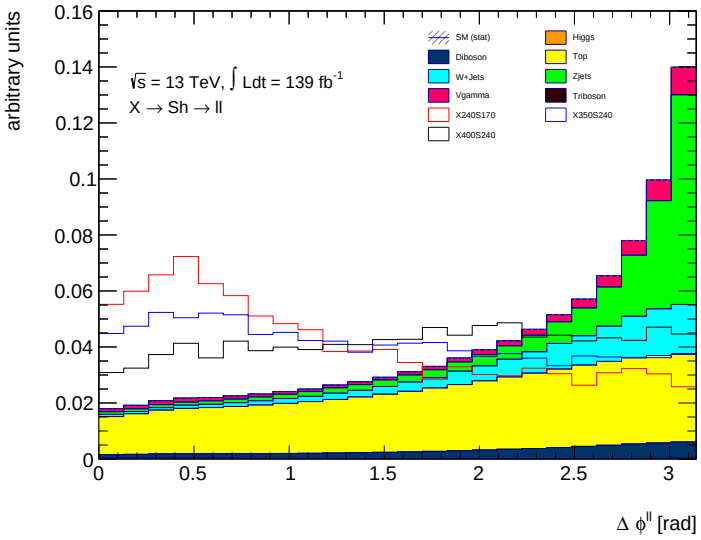

Figure 15: Distributions of $\Delta\phi_{ll}$ in the $e\mu + \mu e$ channel in the main analysis region. The fully colored distributions correspond to yields of different background processes while the empty distributions correspond to the yields of the signal mass points.

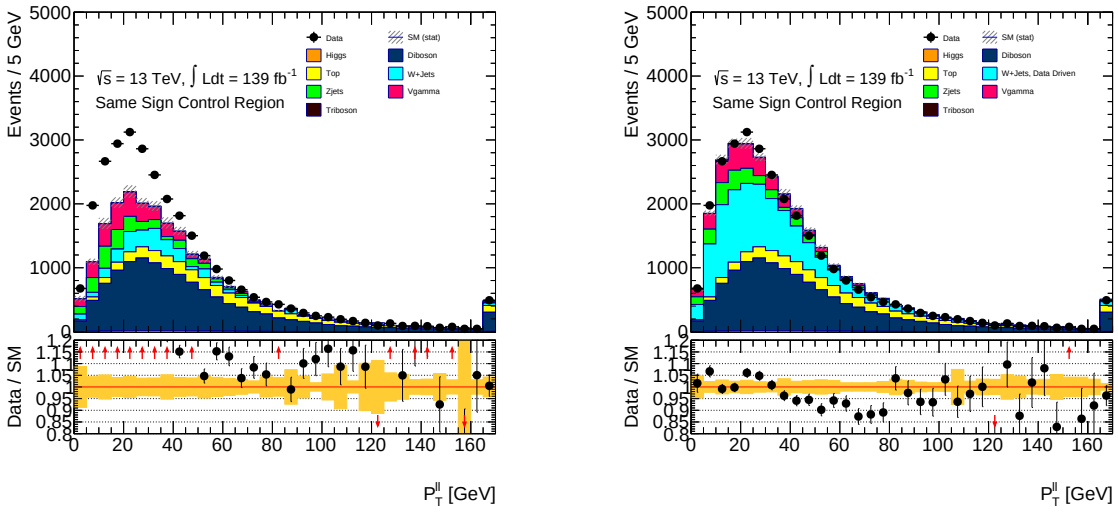

Figure 16: Distributions of the dilepton transverse momentum in the same sign control region using W+jets from MC simulation (left) and from the estimation of the data-driven fake factor method (right). The fully colored distributions correspond to yields of different background processes and black dots represent data yields. The bottom panels present the ratio of data and MC yields.

7.7 Closure test

In order to get further confirmation of the accuracy of the fake factor method, a closure test can be conducted. It is performed by applying the fake factors to the W+jets MC yields in the ID+anti-ID CR, and comparing the number of events to that of the W+jets

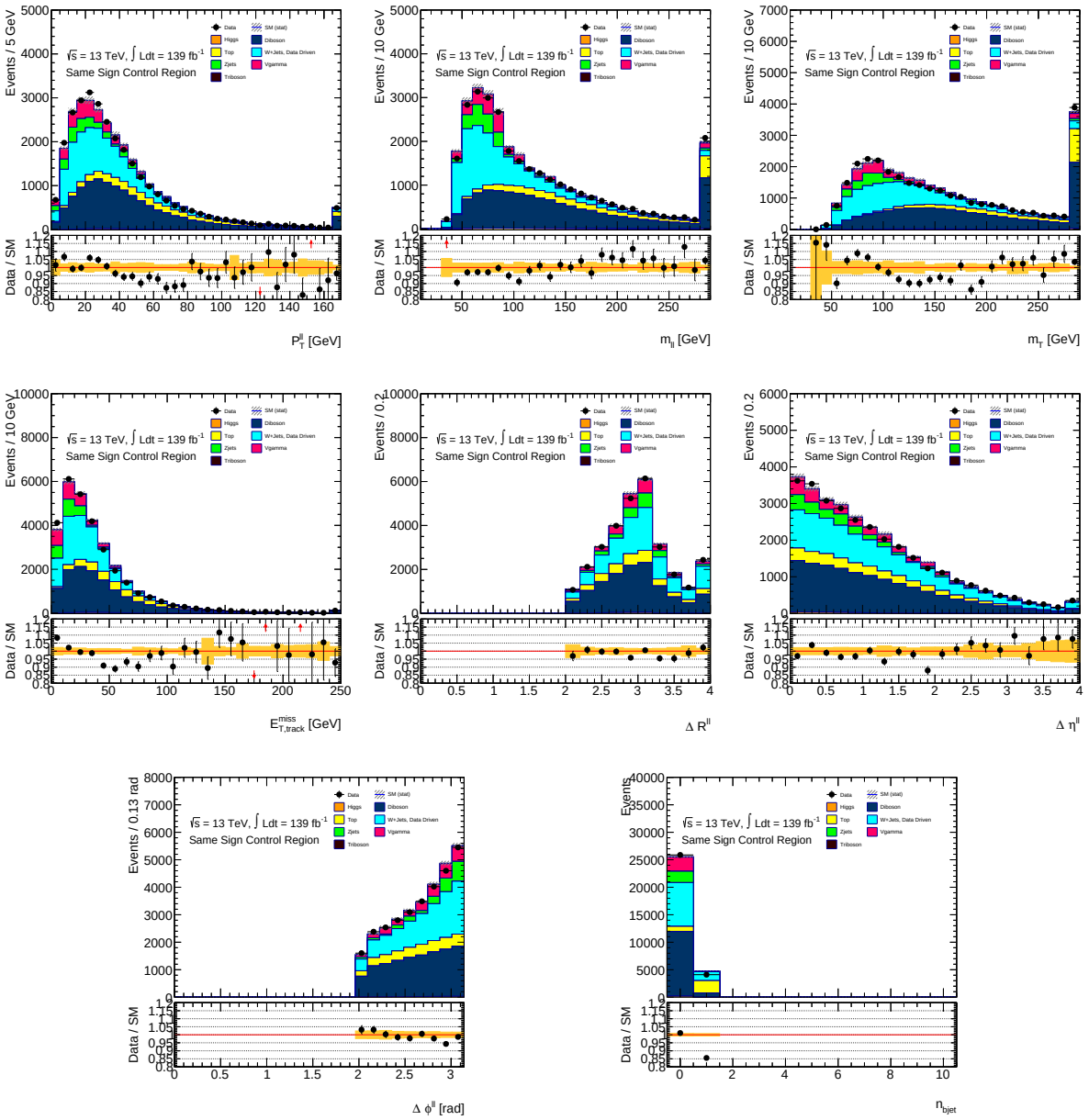

Figure 17: Same sign CR kinematic distributions in the $e\mu+\mu e$ channel after applying the fake factors. The black dots represent data yields while colored bars represent background emerging from different processes. The bottom panels present the ratio of data and MC yields.

MC in the ID+ID signal region (SR). The test is performed at the end of the SR in the dilepton selection. Because there are separate fake factors for each lepton flavor, the W+jets events are split into two parts with respect to each lepton flavor. The closure test is calculated using

$$N_{i,i}^{W+jets(MC)} = F_e \times N_{i,a}^{W+jets(MC),e} + F_\mu \times N_{i,a}^{W+jets(MC),\mu}, \tag{10}$$

where F_e and F_μ are the fake factors, $N_{i,a}^{W+jets(MC),e}$ and $N_{i,a}^{W+jets(MC),\mu}$ are the W+jets MC yields in the anti-ID+ID CR region for the electron and muon respectively and $N_{i,i}^{W+jets(MC)}$ is the W+jets MC yields in the ID+ID SR. The results of the closure test can be seen in Table 16 where the combined yields of both regions can be compared. The application of fake factors in the CR resulted in the combined W+jets yields that is well within the statistical uncertainties of the SR W+jets yields. The relative difference between SR W+jets yields and the CR W+jets yields with the fake factors applied is approximately 2%. The relatively large uncertainty in the CR W+jets yields can be attributed mostly to the uncertainty in the muon fake factor (see Table 15).

Table 16: The first section of the table shows the yields of the W+jets MC in the ID+anti-ID CR with and without application of the fake factors F_l. The lower section shows the yields of W+jets MC in the ID+ID SR region.

Lepton flavor	W+jets MC (anti-ID+ID)	$F_l \times W$+jets MC (anti-ID+ID)
Electron	36532.80 ± 607.54	4639.67 ± 880.20
Muon	39403.23 ± 590.55	1615.53 ± 682.54
Combined	75936.03 ± 847.26	6255.20 ± 1113.83
Lepton flavor		W+jets MC (ID+ID)
Combined		6361 ± 250.15

7.8 Investigation of Flavor Composition

One of the assumptions of the fake factor method is that fake leptons originate from similar sources for both W+jets and Z+jets processes. If the fakes stem from very different sources, the probabilities of being identified as ID or anti-ID would be different between the samples, resulting in disparities in the fake factors. In order to confirm that the fakes originate from similar sources for both W+jets and Z+jets MC samples, a flavor composition study is conducted. This is done by inspecting the truth origin of the fake leptons from MC simulation, where "truth" refers to the true particle a reconstructed object corresponds to. To find the fake composition of Z+jets fakes, the same selection

described in Section 7.3 is used and the truth origin is examined for both the electron and muon in the ID and anti-ID regions. In the case of W+jets, the event selection presented in Section 6.2 is used where an ID and an anti-ID region is set up. Given that prompt leptons originate from W bosons, the remaining lepton which is not associated with the W decay is considered the fake lepton. Such events are examined for the electron and muon in the regions where either both leptons pass ID (ID+ID), or one passes ID and one anti-ID (ID+AID).

Figures 22 and 23 in Appendix B show the fake flavor composition for W+jets and Z+jets respectively. The relevant truth origins corresponding to each bin are presented in Table 25 in Appendix C. The approximate relative contribution from each origin is presented in Table 17 for electron fakes, and in Table 18 for muon fakes. Heavy flavor corresponds to events originating from hadrons including heavy quarks, such as bottom, strange and charm quarks. Light flavor corresponds to events originating from hadrons containing light quarks, such as up and down quarks. As can be seen in Table 17, the contributions agree well and heavy flavor is the dominant contribution for both W+jets and Z+jets samples. Photon conversion is a major component in the full ID region while light flavor is more prevalent in the ID+anti-ID region. The variance in origins for electron fakes is somewhat expected, as there exists a large number of ways to misidentify an electron compared to a muon (see Section 6.1). This is also reflected in Table 18, where the contributions agree more between W+jets and Z+jets samples. Heavy flavor is consistently the dominant contribution, at around 90%. The origins of the fakes show good agreement, and using the fake factor method is thus well justified. This is also supported by the same sign region confirmation and the closure test.

Table 17: Table showing the origins of fakes in the electron ID and anti-ID regions for the W+jets and Z+jets processes.

	W+jets(ID+ID)	Z+jets(ID+ID)	W+jets(ID+AID)	Z+jets(ID+AID)
Photon Conversion	31%	21%	4%	3%
Heavy Flavor	43%	42%	61%	52%
Light Flavor	14%	24%	27%	35%
Other	11%	13%	8%	9%

Table 18: Table showing the origins of fakes in the muon ID and anti-ID regions for the W+jets and Z+jets processes.

	W+jets(ID+ID)	Z+jets(ID+ID)	W+jets(ID+AID)	Z+jets(ID+AID)
Photon Conversion	0%	0%	0%	0%
Heavy Flavor	85%	92%	90%	93%
Light Flavor	7%	4%	7%	4%
Other	8%	6%	3%	3%

7.9 Fake Estimation in the Main Analysis Region

Although W+jets only is the fourth largest contributor to the total background, it is still important that it is modeled accurately. The main reason for this is that W+jets contributes the most in lower m_{ll} regions where the signal is also confined. Figure 18 shows normalized distributions of the dilepton invariant mass in the main analysis region where the overlap of the signal and W+jets background is observed. Table 19 shows the contribution of W+jets when using the data driven method compared to using purely MC simulation. The fake contribution is calculated to be 2.3% of the total background.

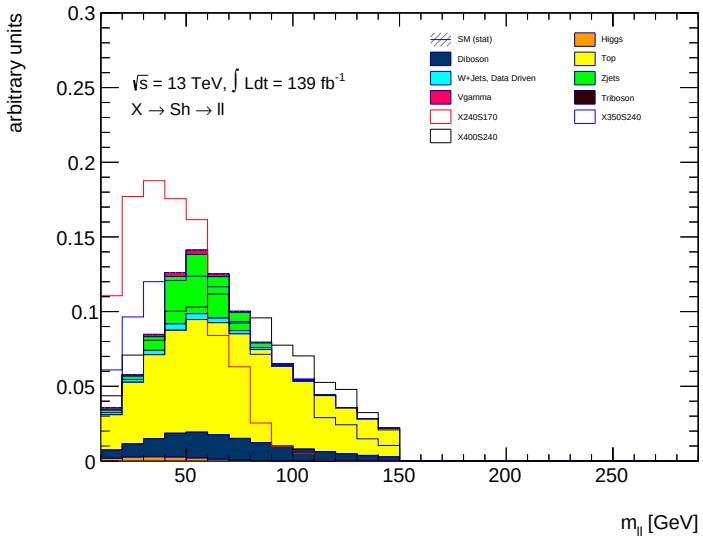

Figure 18: Normalized kinematic distribution of the dilepton invariant mass in the main analysis region. The fully colored distributions correspond to yields of different background processes while the empty distributions correspond to the yields of the signal mass points.

Table 19: Full cutflow of the main analysis in the $e\mu + \mu e$ channel highlighting the differences in yields between using the data driven method for W+jets and purely MC simulation.

$\sqrt{s}$=13 TeV, L=139 fb^{-1} eμ+μe(Full~Run~2)	W+Jets	W+Jets, Data Driven	Total Background
Channel Selection	2438190.18 ± 5024.56	18121533.09 ± 7989.55	23127639.55 ± 9037.83
ID+AID	54016.03 ± 738.83	3501424.62 ± 3696.23	5457177.56 ± 3796.86
Apply Muon FF	54016.03 ± 738.83	1801373.20 ± 2614.54	3757126.14 ± 2754.97
Apply Electron FF	54016.03 ± 738.83	116076.15 ± 263.28	2071829.09 ± 907.40
Trigger Selection	50087.84 ± 710.37	105869.88 ± 252.04	2007068.90 ± 872.88
Trigger Matching	45695.24 ± 666.10	101053.16 ± 229.75	1929989.70 ± 809.06
Overlap: Vgamma/Vjets	40166.48 ± 622.01	103482.37 ± 222.40	1924571.39 ± 764.02
$p_t^{lead} > 22$ GeV	40166.48 ± 622.01	103482.37 ± 222.40	1924571.39 ± 764.02
$p_t^{sublead} > 15$	19031.16 ± 432.83	43320.55 ± 141.27	1697843.19 ± 654.55
$m_{\ell\ell} > 10$ GeV	18881.69 ± 431.01	41759.74 ± 140.14	1693537.75 ± 649.91
OS Leptons	14772.80 ± 381.53	26590.71 ± 116.23	1634844.45 ± 593.61
DL1r: $N_{b\text{-}jet} \leq 1$	14764.83 ± 381.51	25821.65 ± 111.72	1187839.33 ± 576.39
$m_{\ell\ell} < 150$ GeV	12961.28 ± 356.68	24104.95 ± 108.46	947199.94 ± 557.15
$\Delta\eta^{ll} < 1.5$	9756.84 ± 310.28	17525.60 ± 97.29	792190.69 ± 524.74
$m_T < 260$ GeV	9695.24 ± 309.25	17526.48 ± 97.10	778101.82 ± 523.82
$\Delta\varphi^{ll} < 2.7$ [rad]	6189.00 ± 246.73	11615.51 ± 70.05	516051.65 ± 354.62

8 Summary and Conclusion

The aim of this thesis is to optimize the selection of the $X \to Sh \to e^{\pm}\mu^{\mp}$ analysis in ATLAS. The signature final states of the postulated bosons are similar to a broad range of SM background processes, making them exceedingly difficult to measure. A well optimized selection that effectively distinguishes signal events from the background is therefore key in performing a reliable analysis. The author contributed to the optimization of the analysis through three separate studies: the selection of lepton isolation working points, the optimization of the event selection, and the estimation of the W+jets process using the fake factor method. All studies were performed using the same set of MC simulated samples and data collected using the ATLAS detector during Run 2 of the LHC.

Restrictions on the isolation are important as they limit the amount of misidentified leptons that enter the analysis. There exists a wide variety of working points that have varying performance depending on the analysis, and each was evaluated based on the signal significance. The best performing combination of isolation working points is found to be FCTight for both leptons.

The event selection plays a major role in the rejection of background and subsequently the strength of the signal. Different threshold requirements on kinematic quantities allows for the selection of events that contribute to the signal. Because of the interdependency of kinematic quantities, a multidimensional scan is performed that evaluates combinations of cuts based on the approximate Poisson significance. An event selection is determined, where threshold cuts on $m_{ll} < 150$ GeV, $m_{\mathrm{T}} < 260$ GeV, $\Delta\phi_{ll} < 2.7$, $\Delta\eta_{ll} < 1.5$ and $n_{b\mathrm{jet}} < 2$ are applied.

Lepton misidentification due to detector inefficiencies is difficult to simulate using MC, and is instead accounted for using the data driven fake factor method. The fake factor is calculated in a trilepton selection using Z+jets with two prompt leptons and one fake, and is applied to W+jets processes in the main analysis. The accuracy of the fake factors is evaluated using a closure test, where the relative difference between the yields in the full ID region and the anti-ID region with applied fake factors are found to be approximately 2%. The flavor composition of fake leptons in W+jets and Z+jets are investigated and found to be sufficiently consistent.

8.1 Outlook

The work performed in this thesis serves as a contribution to the ongoing $X \rightarrow Sh$ analysis. The selection and optimization performed establishes a foundation that can be incorporated in the main analysis. Although the fake factor method used in this thesis gives good agreements, there exist more sophisticated methods. For example, the fake factor can be calculated for different ranges of p_{T} to obtain improved accuracy, and is something that can be considered in the future.

References

[1] The ATLAS Collaboration, 2012, *Observation of a new particle in the search for the Standard Model Higgs boson with the ATLAS detector at the LHC*, Phys.Lett. B716 (2012) 1-29
arxiv.org/abs/1207.7214

[2] The CMS Collaboration, 2012, *Observation of a new boson at a mass of 125 GeV with the CMS experiment at the LHC*, Phys. Lett. B 716 (2012) 30
arxiv.org/abs/1207.7235

[3] D. J. Griffiths, 2004, *Introduction to elementary particles*, WILEY-VCH Verlag GmbH & Co. KGaA, Weinheim.

[4] M. Tanabashi et al., 2018, *Review of Particle Physics*, Phys. Rev. D 98, 030001
DOI: 10.1103/PhysRevD.98.030001.

[5] S. Abachi et al., 1995, *Observation of the Top Quark*, Phys.Rev.Lett.74:2632-2637
arxiv.org/abs/hep-ex/9503003

[6] K. Kodoma et al., 2000, *Observation of Tau Neutrino Interactions*, Phys.Lett.B504:218-224
arxiv.org/abs/hep-ex/0012035

[7] CERN, *The Standard Model*, home.cern/science/physics/standard-model, visited 2020-09-14

[8] C. Bugard, 2016, *Example: Standard model of physics*, https://texample.net/tikz/examples/model-physics/, visited 2020-09-14

[9] R Nave, Fundamental Forces, hyperphysics.phy-astr.gsu.edu/hbase/Forces/funfor.html, visited 2020-09-15

[10] W. Murray, V. Sharma, 2015, *Properties of the Higgs Boson Discovered at the Large Hadron Collider*, Ann. Rev. Nucl. Part. Sci. 65 (2015) 515-554
DOI:10.1146/ANNUREV-NUCL-102313-025603

[11] J. Ellis, M. K. Gaillard, D. V. Nanopoulos, 2015, *An Updated Historical Profile of the Higgs Boson*
arXiv:1504.07217

[12] G. Sterman, 1993, *An Introduction to Quantum Field Theory*, Cambridge University Press, Cambridge

[13] S. Buddenbrock et al., 2015, *The compatibility of LHC Run 1 data with a heavy scalar of mass around 270 GeV*
arXiv:1506.00612

[14] S. Buddenbrock et al., 2016, *Phenomenological signatures of additional scalar bosons at the LHC*, Eur. Phys. J. C (2016) 76:580
arXiv:1606.01674

[15] S. Buddenbrock et al., 2018, *Multi-lepton signatures of additional scalar bosons beyond the Standard Model at the LHC*
arXiv:1711.07874

[16] S. Buddenbrock et al., 2019, *The emergence of multi-lepton anomalies at the LHC and their compatibility with new physics at the EW scale*, JHEP10(2019)157
arXiv:1901.05300

[17] Y. Hernandez et al., 2019, *The anomalous production of multi-leptons and its impact on the measurement of Wh production at the LHC*
arXiv:1912.00699

[18] LHC Higgs Cross Section Working Group, 2020, https://twiki.cern.ch/twiki/bin/view/LHCPhysics/LHCHXSWG#Higgs_cross_sections_and_decay_b, visited 2020-11-26

[19] ATLAS Collaboration, 2017, *Search for dark matter in association with a Higgs boson decaying to two photons at* $\sqrt{s}$*= 13 TeV with the ATLAS detector*, Phys. Rev. D 96 (2017) 112004
arXiv:1706.03948

[20] L. Evans, P. Bryant, 2008, *LHC Machine*, JINST3 S08001
iopscience.iop.org/article/10.1088/1748-0221/3/08/S08001/meta

[21] E. Mobs, 2019, The CERN accelerator complex, https://cds.cern.ch/record/2684277, visited 2020-10-22

[22] The ALICE Collaboration, 2008, *The ALICE experiment at the CERN LHC*, JINST 3 S08002
https://cds.cern.ch/record/1129812/

[23] The LHCb Collaboration, 2008, *The LHCb experiment at the CERN LHC*, JINST 3 S08005
https://cds.cern.ch/record/1129809

[24] The CMS Collaboration, 2008, *The CMS experiment at the CERN LHC*, JINST 3 S08004
https://cds.cern.ch/record/1129810

[25] The ATLAS Collaboration, 2008, *The ATLAS Experiment at the CERN Large Hadron Collider*, JINST 3 S08003
https://cds.cern.ch/record/1129811

[26] The ATLAS Collaboration, 2014, *Operation and performance of the ATLAS semiconductor tracker*, Nuclear Instruments and Methods in Physics Research A 578 (2007) 98–118
arXiv:1404.7473

[27] The ATLAS Collaboration, 2017, *Performance of the ATLAS Transition Radiation Tracker in Run 1 of the LHC: tracker properties*, JINST 12 (2017) P05002
arXiv:1702.06473

[28] N.J. Buchanan et al., 2008, *Design and implementation of the Front End Board for the readout of the ATLAS liquid argon calorimeters*, JINST 3 (2008) P03004
https://iopscience.iop.org/article/10.1088/1748-0221/3/03/P03004

[29] M. Z. Nedden, 2016, *The LHC Run 2 ATLAS Trigger System:Design, Performance and Plans*,
https://cds.cern.ch/record/2238679

[30] R. Alemany-Fernandez et al., 2013, *Operation and Configuration of the LHC in Run 1*, **Internal Note**

[31] R. Steerenberg et al., 2019, *Operation and performance of the CERN Large Hadron Collider during proton Run 2*
DOI: 10.18429/JACoW-IPAC2019-MOPMP031

[32] The ATLAS Collaboration, Data Quality Information for Data, https://twiki.cern.ch/twiki/bin/view/AtlasPublic/RunStatsPublicResults2010#Full_Run_2_period_2015_2018, visited 2020-12-10

[33] The ATLAS Collaboration, *ATLAS Experiment - Public results*, https://twiki.cern.ch/twiki/bin/view/AtlasPublic/LuminosityPublicResultsRun2, visited 2020-11-04

[34] P. Nason, C. Oleari, 2009, *NLO Higgs boson production via vector-boson fusion matched with shower in POWHEG*, JHEP 1002:037,2010
arXiv:0911.5299

[35] T. Sjöstrand et al., 2016, *PYTHIA 6.4 Physics and Manual*, JHEP 0605:026,2006
arXiv:hep-ph/0603175

[36] H. Lai et al., 2010, *New parton distributions for collider physics*, Phys. Rev. D 82, 074024
DOI: doi.org/10.1103/PhysRevD.82.074024

[37] The ATLAS Collaboration, 2014, *Measurement of the $Z/\gamma*$ boson transverse momentum distribution in pp collisions at $\sqrt{s} = 7$ TeV with the ATLAS detector*, JHEP09(2014) 145
arXiv:1406.3660

[38] J. Alwall et al., 2011, *MadGraph 5 : Going Beyond*
arXiv:1106.0522

[39] The ATLAS Collaboration, 2014, *ATLAS Pythia 8 tunes to 7 TeV data* ATL-PHYS-PUB-2014-021
https://cds.cern.ch/record/1966419

[40] T. Gleisberg et al., 2009, Event generation with SHERPA 1.1, JHEP02(2009) 007
arXiv:0811.46222764[hep-ph]

[41] S. Addepalli et al., 2020, *Measurements of the Higgs boson production cross section via ggF and VBF in $H \to WW* \to lvlv$ with 139fb^{-1} of data collected with the ATLAS detector at $\sqrt{s}$=13TeV*, **Internal Note**
https://cds.cern.ch/record/2231811

[42] The ATLAS Collaboration, 2019, *Electron and photon performance measurements with the ATLAS detector using the 2015–2017 LHC proton–proton collision data*, JINST 14 (2019) P12006
DOI: 10.1088/1748-0221/14/12/P12006

[43] The ATLAS Collaboration. 2015, *Muon reconstruction performance in early* $\sqrt{s} = 13$ *TeV data*
https://cds.cern.ch/record/2047831

[44] M. Cacciari, G. P. Salam, 2008, *The anti-*k_t *clustering algorithm*, JHEP 0804:063,2008
arXiv:0802.1189

[45] M. Cacciari, G. P. Salam, G. Soyez, 2011, *FastJet user manual*
arXiv:1111.6097

[46] The ATLAS Collaboration, 2017, *Jet reconstruction and performance using particle flow with the ATLAS Detector*, Eur. Phys. J. C 77 (2017) 466
DOI: 10.1140/epjc/s10052-017-5031-2656

[47] K. G. Tomiwa, 2016, *Performance of Jet Vertex Tagger in suppression of pileup jets and* E_T^{miss} *in ATLAS detector*, Journal of Physics Conference Series 802(1):012012
DOI: 10.1088/1742-6596/802/1/012012

[48] The ATLAS Collaboration, 2016, *Measurements of the Higgs boson production and decay rates andcoupling strengths using pp collision data at* $\sqrt{s} = 7$ *and 8 TeV in the ATLAS experiment*, Eur. Phys. J. C76 (2016) 6
DOI: 10.1140/epjc/s10052-015-3769-y

[49] The ATLAS collaboration, 2020, *ATLAS b-jet identification performance and efficiency measurements with* $t\bar{t}$ *events in pp collisions at* $\sqrt{s} = 13$ *TeV*, Eur. Phys. J. C 79 (2019) 970
DOI: 10.1140/epjc/s10052-019-7450-8

[50] ASG Analysis Release, 2020, https://twiki.cern.ch/twiki/bin/viewauth/AtlasProtected/AnalysisRelease, visited 2020-11-25

[51] The ATLAS Collaboration, 2010, *Data-Quality Requirements and Event Cleaning for Jets and Missing Transverse Energy Reconstruction with the ATLAS Detector in Proton-Proton Collisions at a Center-of-Mass Energy of* $\sqrt{s} = 7$ *TeV*
https://cds.cern.ch/record/1277678

[52] T. Berger-Hryn'ova, K.Nagano, 2014, *Trigger Menu Strategy for Run 2*
https://cds.cern.ch/record/1703730

[53] The ATLAS Collaboration et al., 2020, *Optimization of the $H \rightarrow WW*$ analysis using the full Run 2 dataset*, **Internal Note**

[54] The ATLAS Collaboration, 2019, *Electron and photon performance measurements with the ATLAS detector using the 2015–2017 LHC proton–proton collision data*, JINST 14 (2019) P12006
DOI: 10.1088/1748-0221/14/12/P12006

[55] Recommended Isolation Working Points, 2020, https://twiki.cern.ch/twiki/bin/viewauth/AtlasProtected/RecommendedIsolationWPs, visited 2020-11-30

[56] Isolation Selection Tool, 2020, https://twiki.cern.ch/twiki/bin/viewauth/AtlasProtected/IsolationSelectionTool, visited 2020-11-30

[57] John Alison, 2012, *The Road to Discovery: Detector Alignment, Electron Identification, Particle Misidentification, WW Physics, and the Discovery of the Higgs Boson*
https://cds.cern.ch/record/1536507

A Cutflows

Tables 20 and 21 contain the full cutflow used for the selection of isolation working points for different ranges of m_{ll} in the $e\mu$ and μe channel respectively. The method is explained in Section 6.1. Tables 22 and 23 present the first and second half of the full cutflow used in the fake factor analysis described in Section 7.

Table 20: Full cutflow of the selection used for the optimization of isolation working points in the $e\mu$ channel. Errors are purely statistical.

$\sqrt{s}$=13 TeV, L=139 fb^{-1} eμ(Full~Run~2)	X240S170	X350S240	X400S240	Total Background	W+Jets
Channel Selection	5035.93 ± 76.93	19023.87 ± 200.62	22939.06 ± 232.15	2692134.78 ± 2931.65	514496.11 ± 2213.44
Trigger Selection	4647.67 ± 73.95	18330.68 ± 197.00	22147.62 ± 228.21	2544485.64 ± 2799.34	470221.86 ± 2112.91
Trigger Matching	4350.04 ± 71.06	17555.85 ± 191.98	21232.68 ± 222.70	2352573.46 ± 2549.24	434171.59 ± 2007.12
Overlap: Vgamma/Vjets	4350.04 ± 71.06	17555.85 ± 191.98	21232.68 ± 222.70	2293300.67 ± 2425.34	405302.64 ± 1932.27
$p_t^{lead} > 22$ GeV	4350.04 ± 71.06	17555.85 ± 191.98	21232.68 ± 222.70	2293300.67 ± 2425.34	405302.64 ± 1932.27
$M_{\ell\ell} > 10$ GeV	3331.54 ± 62.19	14952.63 ± 177.32	18183.32 ± 206.29	1783933.56 ± 1848.48	204364.33 ± 1402.60
OS Leptons	2791.07 ± 56.91	11253.41 ± 153.75	13343.26 ± 176.74	1607483.38 ± 1542.35	163223.56 ± 1245.32
DL1r: $N_{b\text{-}jet} \leq 1$	2493.87 ± 53.86	9683.06 ± 142.85	11462.61 ± 164.04	1266692.49 ± 1538.01	163156.00 ± 1245.36
$p_T^{\ell\ell} > 30$ GeV	2044.47 ± 48.79	8372.20 ± 132.96	9992.29 ± 153.12	825881.74 ± 1224.78	125330.70 ± 1076.19
Lepton ID	1617.47 ± 43.33	6753.11 ± 119.58	8157.72 ± 138.50	613316.99 ± 791.92	57202.22 ± 711.63
$M_{\ell\ell} < 50$ GeV	1039.36 ± 34.73	2656.83 ± 74.85	2125.67 ± 70.57	118035.53 ± 349.29	9479.50 ± 294.08
eTight_mTight_0_50	724.92 ± 29.13	1797.66 ± 61.75	1489.32 ± 59.39	80385.20 ± 186.20	1288.98 ± 112.21
eTight_mLoose_0_50	864.81 ± 31.79	2161.97 ± 67.66	1734.47 ± 63.93	93778.28 ± 218.76	2349.07 ± 147.68
eLoose_mTight_0_50	770.52 ± 29.99	1955.16 ± 64.29	1608.28 ± 61.65	88060.01 ± 215.35	2109.60 ± 145.52
eLoose_mLoose_0_50	922.32 ± 32.78	2345.84 ± 70.34	1882.71 ± 66.56	102913.72 ± 249.46	3393.16 ± 180.11
eTight_mTightTrackOnly_0_50	792.44 ± 30.43	2019.69 ± 65.47	1631.83 ± 62.06	88475.99 ± 205.24	1933.95 ± 135.48
eLoose_mTightTrackOnly_0_50	846.72 ± 31.41	2199.43 ± 68.19	1772.23 ± 64.60	97021.06 ± 234.64	2864.75 ± 167.18
50 $GeV < M_{\ell\ell} < 100$ GeV	565.49 ± 25.63	3027.22 ± 80.18	3617.13 ± 92.21	241222.10 ± 582.56	31906.33 ± 529.67
eTight_mTight_50_100	409.84 ± 21.97	2320.88 ± 70.36	2678.55 ± 79.59	161420.38 ± 224.95	2400.72 ± 151.33
eTight_mLoose_50_100	476.03 ± 23.60	2644.35 ± 75.01	3088.80 ± 85.33	187872.92 ± 296.10	5981.55 ± 230.38
eLoose_mTight_50_100	441.66 ± 22.77	2459.44 ± 72.46	2850.46 ± 82.09	171326.58 ± 249.88	3258.51 ± 179.17
eLoose_mLoose_50_100	512.73 ± 24.45	2808.04 ± 77.30	3300.20 ± 88.17	199445.66 ± 320.31	7088.95 ± 254.30
eTight_mTightTrackOnly_50_100	440.06 ± 22.73	2496.35 ± 72.93	2927.30 ± 83.07	177746.13 ± 279.13	5131.46 ± 214.45
eLoose_mTightTrackOnly_50_100	474.92 ± 23.58	2648.63 ± 75.14	3119.77 ± 85.74	188699.64 ± 303.26	6197.66 ± 238.92
100 $GeV < M_{\ell\ell} < 150$ GeV	12.62 ± 3.73	997.68 ± 46.15	2029.79 ± 69.06	130292.86 ± 333.61	11057.30 ± 312.14
eTight_mTight_100_150	11.06 ± 3.51	856.61 ± 42.75	1766.85 ± 64.55	101618.04 ± 130.75	1024.86 ± 98.07
eTight_mLoose_100_150	12.29 ± 3.72	912.11 ± 44.12	1879.08 ± 66.53	112769.33 ± 173.66	2423.60 ± 146.73
eLoose_mTight_100_150	11.06 ± 3.51	909.86 ± 44.09	1823.78 ± 65.54	105263.19 ± 144.37	1341.48 ± 112.75
eLoose_mLoose_100_150	12.29 ± 3.72	967.10 ± 45.45	1938.44 ± 67.54	116830.75 ± 185.77	2804.24 ± 158.73
eTight_mTightTrackOnly_100_150	12.29 ± 3.72	887.10 ± 43.54	1816.47 ± 65.45	108374.34 ± 159.09	1911.61 ± 131.02
eLoose_mTightTrackOnly_100_150	12.29 ± 3.72	940.35 ± 44.86	1873.40 ± 66.43	112291.48 ± 171.99	2288.44 ± 144.11

Table 21: Full cutflow of the selection used for the optimization of isolation working points in the μe channel. Errors are purely statistical.

$\sqrt{s}$=13 TeV, L=139 fb^{-1} μe(Full~Run~2)	X240S170	X350S240	X400S240	Total Background	W+Jets
Channel Selection	4165.32 ± 70.13	16128.32 ± 185.18	19513.11 ± 214.07	4752161.85 ± 5873.77	1923694.07 ± 4510.76
Trigger Selection	3780.66 ± 66.85	15331.58 ± 180.72	18807.22 ± 210.17	4367152.50 ± 5590.21	1759226.86 ± 4311.24
Trigger Matching	3406.33 ± 62.07	14120.90 ± 170.63	17359.13 ± 198.95	3871713.04 ± 5086.04	1555194.09 ± 3951.69
Overlap: Vgamma/Vjets	3406.33 ± 62.07	14120.90 ± 170.63	17359.13 ± 198.95	3634298.04 ± 4807.46	1433327.50 ± 3792.28
$p_t^{lead} > 22$ GeV	3406.33 ± 62.07	14120.90 ± 170.63	17359.13 ± 198.95	3634298.04 ± 4807.46	1433327.50 ± 3792.28
$M_{\ell\ell} > 10$ GeV	2631.16 ± 54.60	11911.01 ± 157.29	14928.49 ± 185.09	1908787.08 ± 2704.10	389727.04 ± 1981.32
OS Leptons	2295.91 ± 51.01	9194.31 ± 138.23	10979.68 ± 158.71	1557462.23 ± 2157.69	251604.82 ± 1595.49
DL1r: $N_{b\text{-}jet} \leq 1$	2066.63 ± 48.47	7878.64 ± 128.22	9408.76 ± 146.92	1266773.04 ± 2154.19	251481.36 ± 1594.99
$p_T^{\ell\ell} > 30$ GeV	1752.45 ± 44.70	6720.70 ± 118.28	8231.01 ± 137.35	821719.55 ± 1704.12	183631.20 ± 1354.57
Lepton ID	1312.86 ± 38.76	5217.12 ± 104.43	6462.11 ± 121.99	474527.33 ± 612.56	26901.81 ± 515.97
$M_{\ell\ell} < 50$ GeV	869.19 ± 31.49	1925.53 ± 63.14	1562.77 ± 59.76	84268.42 ± 271.55	5026.17 ± 219.86
eTight_mTight_0_50	605.63 ± 26.29	1409.20 ± 54.09	1157.56 ± 51.61	59532.14 ± 154.58	916.86 ± 95.34
eTight_mLoose_0_50	665.66 ± 27.58	1507.16 ± 55.90	1207.72 ± 52.68	62850.36 ± 161.57	1110.88 ± 104.11
eLoose_mTight_0_50	745.34 ± 29.12	1681.02 ± 59.02	1401.09 ± 56.64	72997.45 ± 203.01	2082.44 ± 144.23
eLoose_mLoose_0_50	823.81 ± 30.65	1801.32 ± 61.06	1472.08 ± 58.05	77192.23 ± 211.22	2379.35 ± 153.22
eTight_mTightTrackOnly_0_50	642.39 ± 27.08	1482.21 ± 55.48	1181.56 ± 52.11	61878.97 ± 160.00	1056.06 ± 102.22
eLoose_mTightTrackOnly_0_50	791.12 ± 30.02	1776.41 ± 60.68	1437.32 ± 57.33	75972.24 ± 209.22	2290.16 ± 150.94
50 $GeV < M_{\ell\ell} < 100$ GeV	436.82 ± 22.42	2376.88 ± 70.52	2895.24 ± 81.51	174597.38 ± 443.72	14325.24 ± 375.12
eTight_mTight_50_100	334.67 ± 19.73	1834.27 ± 61.99	2239.96 ± 71.71	127332.34 ± 229.47	2717.44 ± 162.35
eTight_mLoose_50_100	353.96 ± 20.31	1892.77 ± 62.94	2321.50 ± 72.93	131582.51 ± 235.08	2929.33 ± 168.28
eLoose_mTight_50_100	399.73 ± 21.43	2188.62 ± 67.72	2630.29 ± 77.68	154295.58 ± 322.81	6398.83 ± 251.20
eLoose_mLoose_50_100	423.52 ± 22.08	2264.65 ± 68.84	2732.28 ± 79.14	159466.79 ± 328.65	6720.48 ± 256.97
eTight_mTightTrackOnly_50_100	350.08 ± 20.19	1881.53 ± 62.75	2308.41 ± 72.77	130207.86 ± 232.95	2847.39 ± 165.89
eLoose_mTightTrackOnly_50_100	418.57 ± 21.94	2248.53 ± 68.60	2714.17 ± 78.91	157789.07 ± 326.21	6577.76 ± 254.33
100 $GeV < M_{\ell\ell} < 150$ GeV	6.86 ± 2.83	833.11 ± 42.12	1666.09 ± 62.15	105287.94 ± 258.55	4962.92 ± 225.41
eTight_mTight_100_150	6.86 ± 2.83	720.90 ± 39.23	1408.14 ± 57.25	86558.06 ± 139.17	999.03 ± 102.85
eTight_mLoose_100_150	6.86 ± 2.83	744.92 ± 39.85	1429.69 ± 57.70	88092.97 ± 142.13	1059.27 ± 105.94
eLoose_mTight_100_150	6.86 ± 2.83	789.92 ± 41.07	1592.53 ± 60.76	98810.32 ± 194.23	2562.73 ± 161.28
eLoose_mLoose_100_150	6.86 ± 2.83	815.87 ± 41.71	1614.53 ± 61.19	100562.44 ± 197.41	2639.72 ± 164.40
eTight_mTightTrackOnly_100_150	6.86 ± 2.83	732.83 ± 39.54	1429.08 ± 57.68	87674.95 ± 140.77	1047.19 ± 104.56
eLoose_mTightTrackOnly_100_150	6.86 ± 2.83	803.92 ± 41.42	1613.47 ± 61.17	100077.00 ± 196.27	2620.04 ± 163.33

Table 22: First half of the full cutflow of the Z+jets fake factor analysis. The errors are purely statistical.

$\sqrt{s}$=13 TeV, L=139 fb^{-1} 3((Full~Run~2)	Zjets	WZ	WW	ZZ	Top
Channel Selection	818912.69 ± 482.29	60324.80 ± 1687.17	2571.53 ± 13.96	26557.39 ± 123.47	152785.07 ± 82.04
Jet Cleaning	818912.69 ± 482.29	60324.80 ± 1687.17	2571.53 ± 13.96	26557.39 ± 123.47	152785.07 ± 82.04
Overlap: Vgamma/Vjets	645400.29 ± 430.69	60324.80 ± 1687.17	2571.53 ± 13.96	26557.39 ± 123.47	152785.07 ± 82.04
$p_t^{all} > 15$ GeV	203100.57 ± 239.45	46798.65 ± 1684.86	902.00 ± 7.76	14204.88 ± 111.99	81247.85 ± 59.43
m+m+m	24912.61 ± 92.39	16529.63 ± 1683.77	36.39 ± 1.36	4527.40 ± 35.52	16498.81 ± 26.59
mmml011 Z-tagging	11279.54 ± 61.11	5876.74 ± 15.91	8.17 ± 0.66	809.50 ± 12.61	3703.66 ± 12.35
ID Z-pair	8592.69 ± 53.37	4689.36 ± 14.23	4.11 ± 0.48	588.05 ± 11.25	1224.32 ± 6.66
MT < 50 GeV	7192.51 ± 48.90	1671.13 ± 8.55	1.80 ± 0.34	394.20 ± 7.54	527.65 ± 4.48
mmml2 Fake ID	277.89 ± 9.53	1361.36 ± 7.82	0.16 ± 0.08	267.43 ± 3.53	100.27 ± 1.14
mmml2 Fake Anti-ID	6285.75 ± 45.96	230.89 ± 2.96	1.11 ± 0.27	110.65 ± 6.59	400.97 ± 4.22
mmml011 Z-tagging	12744.08 ± 65.65	5952.03 ± 37.31	9.79 ± 0.70	1508.83 ± 16.31	4978.80 ± 14.49
ID Z-pair	8454.88 ± 53.08	4184.15 ± 14.38	3.41 ± 0.34	980.74 ± 10.77	1780.01 ± 8.45
MT < 50 GeV	7008.57 ± 48.41	1143.67 ± 8.23	1.45 ± 0.24	672.30 ± 9.41	534.25 ± 4.64
mmml1 Fake ID	401.13 ± 11.66	913.90 ± 7.58	0.06 ± 0.04	436.53 ± 6.07	57.96 ± 1.01
mmml1 Fake Anti-ID	5884.73 ± 44.57	174.65 ± 2.89	1.32 ± 0.23	205.46 ± 6.99	448.39 ± 4.40
e+e+m	19339.85 ± 79.66	9739.92 ± 22.45	386.62 ± 4.82	3222.82 ± 24.13	24309.36 ± 32.64
eeml011 Z-tagging	8218.10 ± 47.99	4143.15 ± 15.55	19.55 ± 1.07	565.95 ± 7.76	1935.71 ± 8.75
ID Z-pair	5668.38 ± 39.76	2977.93 ± 12.55	4.19 ± 0.50	389.45 ± 6.47	886.31 ± 5.68
MT < 50 GeV	5086.73 ± 37.80	1064.88 ± 6.53	1.57 ± 0.32	268.88 ± 5.98	423.73 ± 4.06
eeml2 Fake ID	180.70 ± 7.13	862.85 ± 5.91	0.04 ± 0.02	177.52 ± 4.58	73.61 ± 0.97
eeml2 Fake Anti-ID	4490.34 ± 35.64	154.70 ± 2.44	1.39 ± 0.31	81.50 ± 3.78	331.06 ± 3.85
eeml012 Z-tagging	8702.09 ± 50.24	3642.56 ± 12.43	21.23 ± 1.17	1048.65 ± 13.19	2652.99 ± 10.53
ID Z-pair	5497.88 ± 39.51	2346.51 ± 9.83	3.08 ± 0.42	624.47 ± 9.79	1180.93 ± 6.94
MT < 50 GeV	4943.28 ± 37.62	664.80 ± 5.21	1.41 ± 0.29	472.57 ± 9.00	402.61 ± 4.04
eeml1 Fake ID	247.86 ± 8.75	518.48 ± 4.65	0.16 ± 0.12	279.11 ± 6.21	36.50 ± 0.81
eeml1 Fake Anti-ID	4216.48 ± 34.85	114.32 ± 2.09	1.05 ± 0.25	174.43 ± 6.33	346.76 ± 3.86
e+e+e	73608.24 ± 133.06	8237.77 ± 26.97	173.49 ± 3.81	2916.73 ± 20.52	5487.24 ± 15.09
eeel012 Z-tagging	19561.96 ± 68.34	3274.15 ± 21.73	33.08 ± 1.57	825.16 ± 8.47	1124.22 ± 6.66
ID Z-pair	10953.73 ± 51.05	2105.25 ± 12.60	11.17 ± 0.83	516.03 ± 6.20	422.74 ± 3.90
MT < 50 GeV	10324.70 ± 49.58	618.71 ± 6.01	4.08 ± 0.51	404.01 ± 5.74	153.14 ± 2.36
eeel2 Fake ID	328.50 ± 8.98	719.26 ± 6.56	0.04 ± 0.14	209.44 ± 2.62	58.58 ± 0.82
eeel2 Fake Anti-ID	3188.45 ± 27.90	117.00 ± 2.05	1.19 ± 0.28	50.17 ± 2.75	59.53 ± 1.54
eeel011 Z-tagging	19780.86 ± 68.40	3712.62 ± 13.61	27.07 ± 1.22	653.41 ± 9.25	928.68 ± 5.67
ID Z-pair	13466.61 ± 56.53	2680.47 ± 11.07	13.71 ± 0.85	448.71 ± 6.27	408.59 ± 3.37
MT < 50 GeV	12179.58 ± 53.80	992.26 ± 7.36	5.08 ± 0.59	303.07 ± 4.28	175.53 ± 2.28
eeel1 Fake ID	371.93 ± 9.67	424.58 ± 5.38	0.08 ± 0.05	260.81 ± 3.66	29.80 ± 0.69
eeel1 Fake Anti-IDD	3338.23 ± 28.51	92.96 ± 1.82	0.95 ± 0.26	83.98 ± 3.56	65.14 ± 1.65
e+m+m	85239.88 ± 157.33	12291.33 ± 49.45	305.49 ± 4.54	3537.92 ± 101.38	34952.44 ± 39.15
emml012 Z-tagging	24508.62 ± 82.90	4185.01 ± 14.51	32.24 ± 1.68	923.84 ± 7.39	2221.23 ± 9.65
ID Z-pair	16975.33 ± 68.95	3165.04 ± 12.75	14.34 ± 1.23	696.33 ± 6.80	586.31 ± 4.57
MT < 50 GeV	15929.73 ± 66.78	892.86 ± 6.61	5.23 ± 0.77	531.72 ± 5.39	214.70 ± 2.80
emml2 Fake ID	471.37 ± 11.80	990.01 ± 7.20	0.05 ± 0.03	276.73 ± 2.45	74.56 ± 0.90
emml2 Fake Anti-ID	4932.72 ± 37.55	151.95 ± 2.77	1.85 ± 0.42	55.94 ± 2.07	81.71 ± 1.84
emml011 Z-tagging	26235.14 ± 85.73	4615.24 ± 19.19	26.63 ± 1.27	723.57 ± 6.87	1823.05 ± 8.36
ID Z-pair	20355.13 ± 75.53	3720.41 ± 18.23	18.58 ± 1.04	576.50 ± 6.49	546.20 ± 3.92
MT < 50 GeV	18458.81 ± 71.92	1352.48 ± 8.30	6.13 ± 0.71	390.83 ± 5.83	233.25 ± 2.68
emml1 Fake ID	574.93 ± 13.09	612.12 ± 5.43	0.11 ± 0.08	360.52 ± 3.09	41.30 ± 0.80
emml1 Fake Anti-ID	5063.51 ± 38.09	134.82 ± 2.46	1.15 ± 0.42	99.54 ± 3.84	90.68 ± 1.93

Table 23: Second half of the full cutflow of the Z+jets fake factor analysis. The errors are purely statistical.

$\sqrt{s}$=13 TeV, L=139 fb^{-1} 3((Full~Run~2)	W+Jets	Vgamma	Triboson	Higgs	total bkg	Data
Channel Selection	33468.80 ± 565.55	207682.08 ± 1079.34	455.10 ± 3.21	790.99 ± 1.91	1303548.47 ± 2141.53	1831621
Jet Cleaning	33468.80 ± 565.55	207682.08 ± 1079.34	455.10 ± 3.21	790.99 ± 1.91	1303548.47 ± 2141.53	1831621
Overlap: Vgamma/Vjets	24153.15 ± 480.45	207682.08 ± 1079.34	455.10 ± 3.21	790.99 ± 1.91	1120720.41 ± 2109.51	1831621
$p_t^{all} > 15$ GeV	3191.86 ± 175.16	89482.70 ± 792.45	373.07 ± 2.86	449.93 ± 1.27	439751.51 ± 1889.68	563179
m+m+m	386.78 ± 66.27	989.54 ± 70.42	65.83 ± 1.14	91.35 ± 0.55	64038.35 ± 1689.65	104440
mmml011 Z-tagging	0.00	297.06 ± 38.29	22.33 ± 0.54	31.95 ± 0.34	22028.96 ± 75.94	24977
ID Z-pair	0.00	185.70 ± 32.45	17.83 ± 0.49	24.86 ± 0.29	15326.92 ± 65.39	16903
MT < 50 GeV	0.00	129.46 ± 28.86	4.98 ± 0.24	16.10 ± 0.25	9937.82 ± 58.09	11078
mmml2 Fake ID	0.00	6.61 ± 4.34	4.16 ± 0.21	10.89 ± 0.20	2028.77 ± 13.59	2064
mmml2 Fake Anti-ID	0.00	111.65 ± 27.90	0.60 ± 0.11	4.42 ± 0.14	7146.04 ± 54.42	8116
mmml011 Z-tagging	155.57 ± 43.46	438.11 ± 48.56	17.35 ± 0.55	32.73 ± 0.33	25837.29 ± 102.11	36234
ID Z-pair	0.00	158.14 ± 34.71	12.96 ± 0.50	21.50 ± 0.26	15595.78 ± 66.46	18169
MT < 50 GeV	0.00	136.14 ± 29.44	2.86 ± 0.23	9.66 ± 0.19	9508.91 ± 58.20	10994
mmml1 Fake ID	0.00	-1.61 ± 4.52	2.24 ± 0.20	6.63 ± 0.15	1816.84 ± 15.86	1811
mmml1 Fake Anti-ID	0.00	114.74 ± 27.26	0.35 ± 0.06	2.62 ± 0.11	6832.28 ± 52.98	8127
e+e+m	1215.57 ± 108.77	2360.12 ± 82.76	123.46 ± 1.70	140.11 ± 0.72	60837.82 ± 164.94	80516
eeml011 Z-tagging	10.41 ± 10.41	206.04 ± 31.16	17.58 ± 0.56	23.17 ± 0.28	15139.66 ± 61.34	17361
ID Z-pair	0.00	110.11 ± 23.17	12.81 ± 0.49	17.02 ± 0.24	10066.21 ± 48.47	11348
MT < 50 GeV	0.00	106.43 ± 23.09	3.74 ± 0.36	11.39 ± 0.21	6967.35 ± 45.36	8045
eeml2 Fake ID	0.00	0.16 ± 0.09	3.18 ± 0.35	7.79 ± 0.16	1305.84 ± 10.38	1239
eeml2 Fake Anti-ID	0.00	98.47 ± 21.32	0.37 ± 0.04	3.03 ± 0.12	5160.85 ± 41.95	6222
eeml012 Z-tagging	52.63 ± 21.69	249.05 ± 41.17	12.26 ± 0.40	23.27 ± 0.29	16404.74 ± 71.63	19830
ID Z-pair	0.00	98.55 ± 16.39	8.25 ± 0.34	12.70 ± 0.19	9772.37 ± 45.51	11390
MT < 50 GeV	0.00	78.74 ± 14.48	1.76 ± 0.15	6.33 ± 0.15	6571.50 ± 41.82	7698
eeml1 Fake ID	0.00	1.29 ± 0.97	1.49 ± 0.14	4.22 ± 0.12	1089.10 ± 11.77	1052
eeml1 Fake Anti-ID	0.00	74.18 ± 14.37	0.21 ± 0.04	1.79 ± 0.09	4929.20 ± 38.47	5912
e+e+e	680.76 ± 77.69	33928.64 ± 388.64	45.25 ± 0.92	64.94 ± 0.50	125143.06 ± 419.73	129648
eeel012 Z-tagging	161.14 ± 37.99	5049.79 ± 149.62	10.10 ± 0.38	17.70 ± 0.25	30057.31 ± 170.57	32033
ID Z-pair	0.00	2758.99 ± 111.67	6.56 ± 0.32	9.95 ± 0.17	16784.42 ± 123.65	17196
MT < 50 GeV	0.00	2442.45 ± 106.99	1.45 ± 0.16	4.85 ± 0.13	13953.40 ± 118.24	13975
eeel2 Fake ID	0.00	60.52 ± 13.95	2.09 ± 0.13	6.31 ± 0.15	1384.75 ± 18.05	1436
eeel2 Fake Anti-ID	0.00	110.72 ± 25.87	0.46 ± 0.13	1.36 ± 0.06	3528.86 ± 38.23	3123
eeel011 Z-tagging	25.00 ± 12.86	3141.26 ± 116.90	12.57 ± 0.37	19.99 ± 0.26	28301.46 ± 137.17	29066
ID Z-pair	0.00	1806.61 ± 88.25	9.34 ± 0.32	14.48 ± 0.22	18848.54 ± 105.63	19202
MT < 50 GeV	0.00	1461.12 ± 83.91	2.83 ± 0.18	9.27 ± 0.18	15128.73 ± 100.07	15105
eeel1 Fake ID	0.00	151.83 ± 24.45	1.14 ± 0.14	3.19 ± 0.11	1243.36 ± 27.10	1278
eeel1 Fake Anti-IDD	0.00	217.65 ± 33.07	0.20 ± 0.07	0.86 ± 0.05	3799.96 ± 43.87	3471
e+m+m	908.75 ± 91.79	52204.40 ± 682.00	138.54 ± 1.78	153.52 ± 0.73	189732.28 ± 715.95	248575
emml012 Z-tagging	64.13 ± 25.38	6855.36 ± 510.93	12.76 ± 0.43	21.25 ± 0.26	38824.43 ± 518.59	40328
ID Z-pair	0.00	5029.55 ± 502.70	9.56 ± 0.37	14.34 ± 0.21	26490.80 ± 507.63	26250
MT < 50 GeV	0.00	3969.10 ± 134.98	2.08 ± 0.17	7.03 ± 0.16	21552.48 ± 150.86	21124
emml2 Fake ID	0.00	131.76 ± 19.00	3.04 ± 0.21	8.44 ± 0.18	1955.97 ± 23.64	1944
emml2 Fake Anti-ID	0.00	158.49 ± 30.86	0.42 ± 0.08	1.91 ± 0.08	5385.00 ± 48.77	4685
emml011 Z-tagging	8.64 ± 8.64	3483.80 ± 124.04	16.72 ± 0.43	24.24 ± 0.29	36957.04 ± 152.63	38095
ID Z-pair	0.00	2651.16 ± 106.38	13.25 ± 0.38	19.47 ± 0.26	27900.71 ± 131.95	28174
MT < 50 GeV	0.00	2139.11 ± 97.40	4.00 ± 0.25	12.38 ± 0.22	22596.99 ± 121.53	22164
emml1 Fake ID	0.00	154.08 ± 26.09	1.52 ± 0.15	4.48 ± 0.13	1749.05 ± 29.87	1776
emml1 Fake Anti-ID	0.00	407.88 ± 42.43	0.33 ± 0.07	1.27 ± 0.07	5799.19 ± 57.24	5204

B Figures

Figures 19 and 20 show the normalized kinematic distributions and significance scan in the $e\mu + \mu e$ channel for the $X350S240$ and $X400S240$ signal mass points respectively. Their use is discussed in Section 6.2. Figure 21 shows the kinematic distributions in the SS CR without the application of the fake factors. For comparison, Figure 17 in Section 7.6 shows the same distributions with the fake factors applied. The methodology is explained in Section 7. Figures 22 and 23 show the origins of reconstructed leptons for W+jets and Z+jets respectively. Table 25 in Appendix C show the relevant origins corresponding to the bins in the plots. The origins and flavor composition is discussed in Section 7.8.

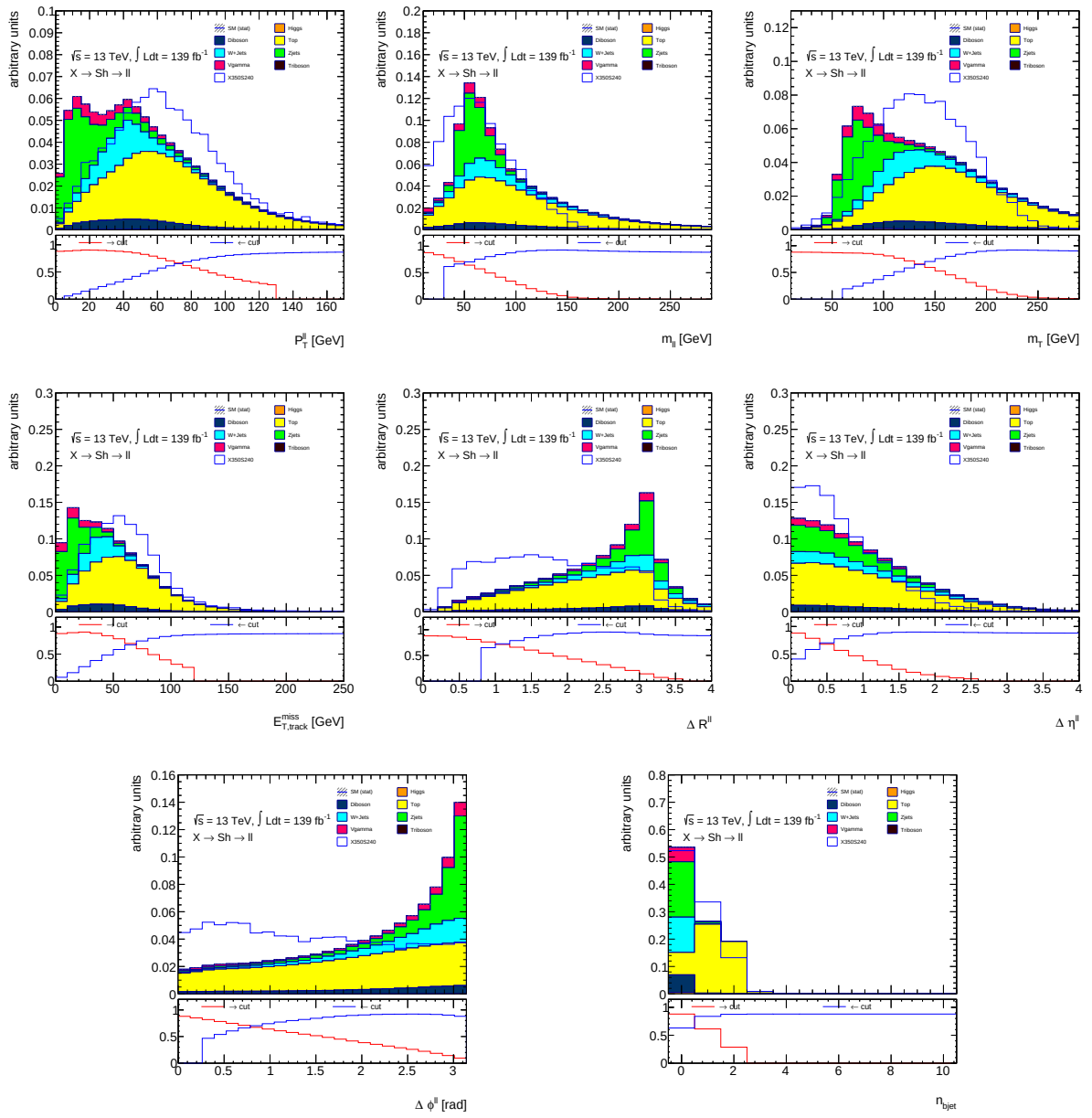

Figure 19: Normalized kinematic distributions and significance scan in the $e\mu+\mu e$ channel where the signal yields correspond to the $X350S240$ mass point.

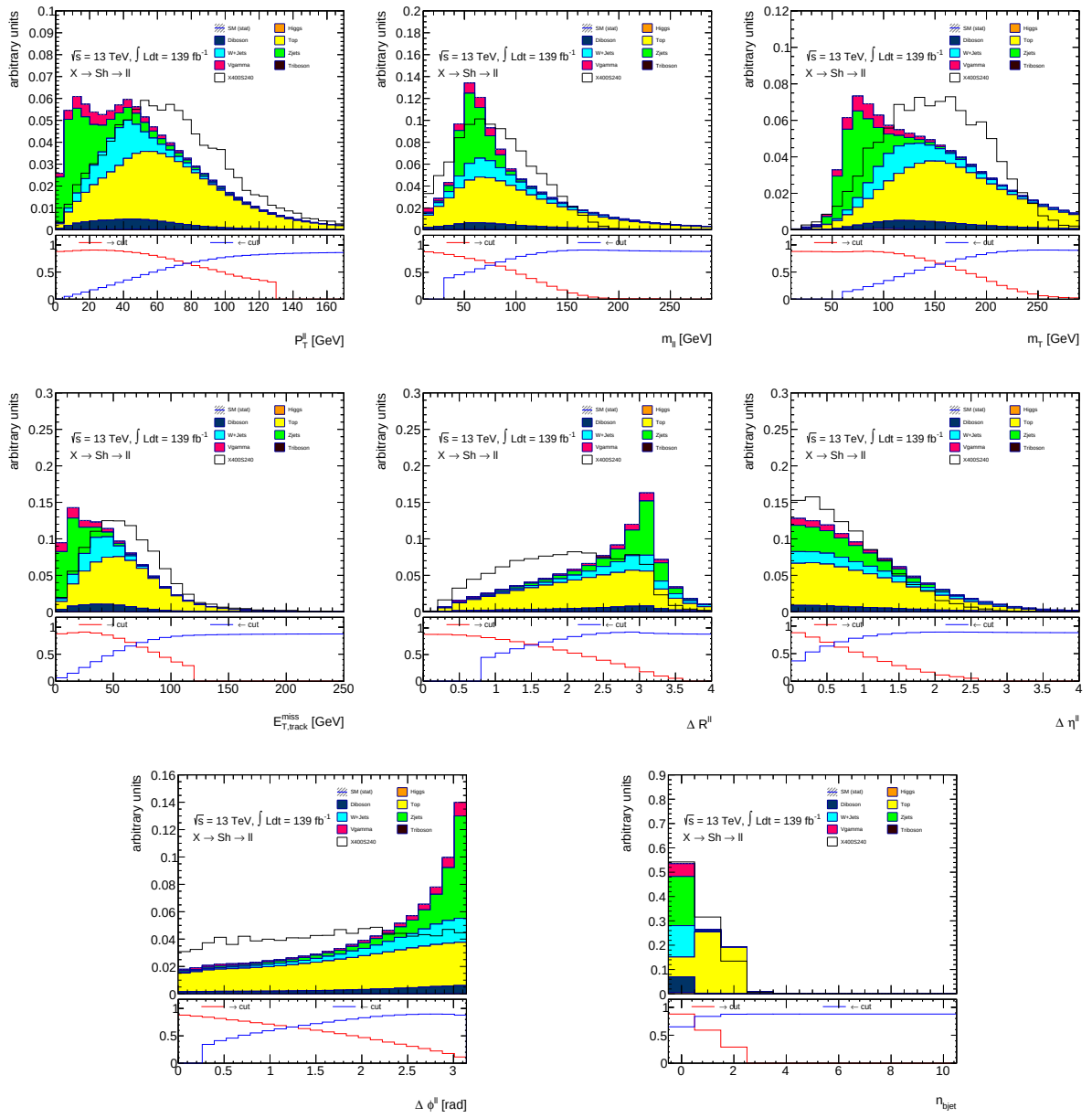

Figure 20: Normalized kinematic distributions and significance scan in the $e\mu+\mu e$ channel where the signal yields correspond to the $X400S240$ mass point.

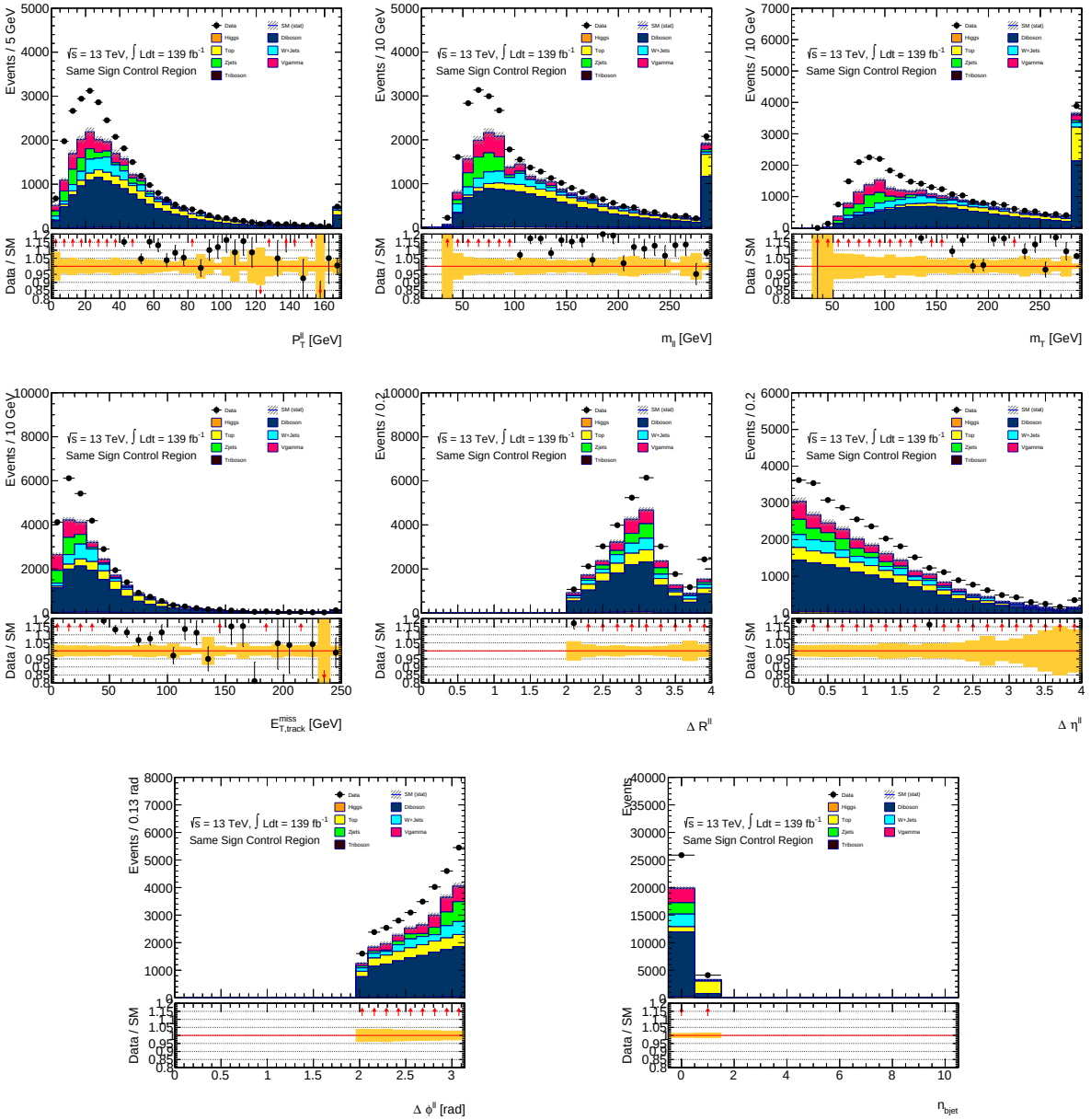

Figure 21: Kinematic distributions in the SS CR without the application of the fake factor method.

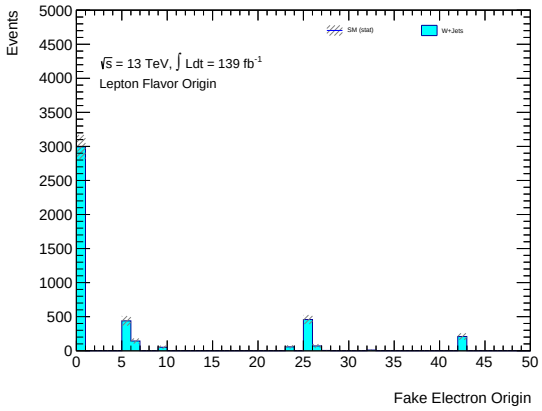

(a) ID+ID region truth origin for the electron.

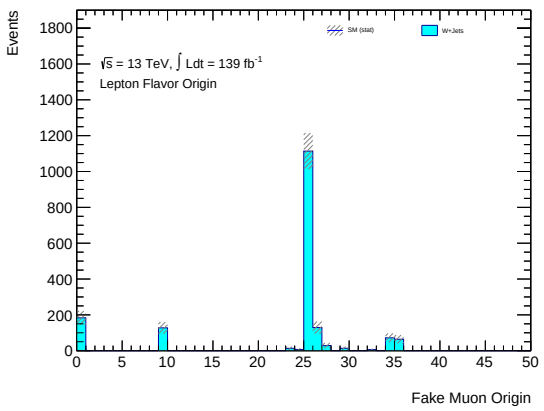

(b) ID+ID region truth origin for the muon.

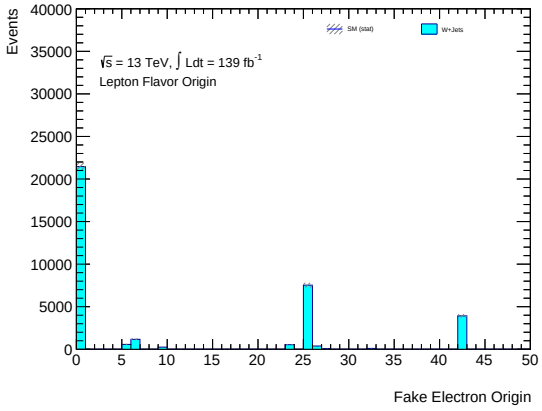

(c) ID+anti-ID region truth origin for the electron.

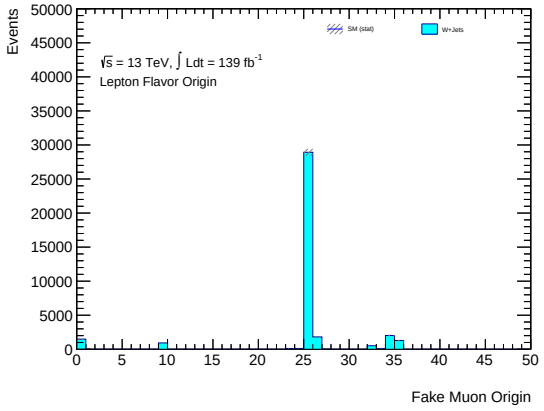

(d) ID+anti-ID region truth origin for the muon.

Figure 22: Truth origin of electron and muon fakes from W+jets processes in the ID+ID and ID+anti-ID regions.

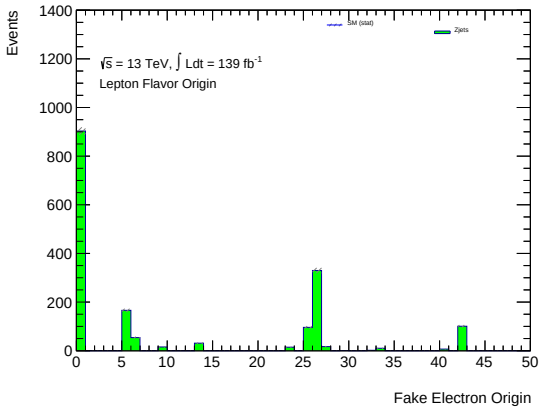

(a) ID+ID region truth origin for the electron.

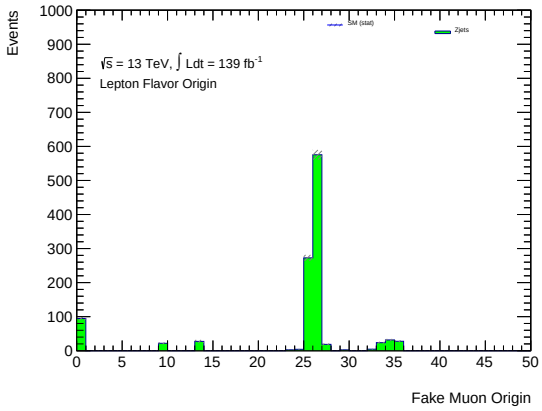

(b) ID+ID region truth origin for the muon.

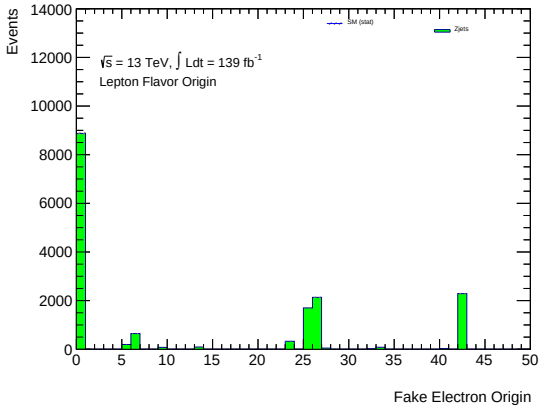

(c) ID+anti-ID region truth origin for the electron.

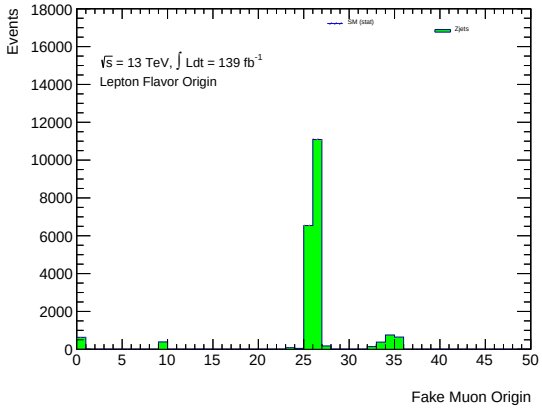

(d) ID+anti-ID region truth origin for the muon.

Figure 23: Truth origin of electron and muon fakes from Z+jets processes in the Z+ID and Z+anti-ID regions.

C Tables

Table 24 shows the fake factor for each fake lepton category. The method of obtaining the fake factors is explained in Section 7. Table 25 shows the relevant origins corresponding to each bin in Figures 22 and 23.

Table 24: Numerical results of the fake factors for the different fake candidate categories. The uncertainties are only statistical.

Fake Candidate Flavor	Category	Fake Factor
Muon	mmml1	0.055 ± 0.002
	mmml2	0.043 ± 0.001
	eeml1	0.041 ± 0.001
	eeml2	0.021 ± 0.001
Electron	eeel1	0.145 ± 0.011
	eeel2	0.112 ± 0.009
	emml1	0.135 ± 0.008
	emml2	0.109 ± 0.008

Table 25: The bins corresponding to relevant truth origins.

Bin	Truth Origin
0	Unknown
5	Photon Conversion
6	Dalitz Decay
9	Tau Lepton
13	Z boson
23	Light Meson
24	Strange Meson
25	Charmed Meson
26	Bottom Meson
32	Charmed Baryon
33	Bottom Baryon
34	Pion Decay
35	Kaon Decay
42	π_0